
TECHNICAL REPORT R-98

HOT-WIRE CALORIMETRY: THEORY AND APPLICATION TO ION ROCKET RESEARCH

By LIONEL V. BALDWIN and VIRGIL A. SANDBORN

**Lewis Research Center
Cleveland, Ohio**

TECHNICAL REPORT R-98

HOT-WIRE CALORIMETRY: THEORY AND APPLICATION TO ION ROCKET RESEARCH

By LIONEL V. BALDWIN and VIRGIL A. SANDBORN

SUMMARY

A very small calorimeter probe (0.001 by 0.25 cm) for measuring local power density in high-energy ion beams has been studied both theoretically and experimentally. For high sensitivity, the wire is heated by a detection current; the change in wire temperature due to ion impingement results in a voltage output. Both ion and joulean heat inputs are balanced by conduction along the wire to cooled supports. A steady-state calibration and error analysis is supported by experiment. Power-density measurements in 1- to 20-kilovolt cesium and mercury ion beams are presented as detailed spatial profile and contour maps. An analysis for the transient response of the hot-wire calorimeter was also verified by calibration experiments. Although not experimentally explored, several additional future applications are discussed: power-density fluctuation measurements from 0 to 10,000 cycles per second, ion velocity vector determination using yawed wires for direction finding, and a time of flight technique for velocity magnitude.

INTRODUCTION

One of the possible propulsion systems for space flight now being studied experimentally is the ion rocket. In an ion rocket, the propellant is ionized and accelerated by an electrostatic field. The ion beam exhausts at about 20,000 to 200,000 meters per second into a neutralization region where ideally an equal current of electrons is injected into the beam to eliminate space charge outside the rocket. The interest in ion rockets stems from their potential for supplying extremely high values of specific impulse. Reference 1 reviews the general characteristics of these low-thrust systems and references 2 to 4 discuss some of the experimental

facilities and research engines of the NASA program.

Research with experimental ion rocket engines requires the measurement of ion-beam momentum, power, velocity, and current density (or mass-flow rate per unit area). These are not independent quantities, and the measurement of two of these quantities will permit calculation of the remaining values. In the ion rockets under study for possible space flight application some optimum value of ion velocity usually exists (ref. 1). All the ions should emerge at this velocity (except for charge exchange ions), since they fall from some fixed positive potential at the ion emitter to ground potential outside the engine. Thus, ion velocities are known from the measurement of emitter voltage, and a measurement of the beam power density should permit accurate computation of current density or mass-flow rate per unit area.

In addition to the overall or average values of the beam power and current density, the variation of these performance characteristics with location in the beam is also of considerable interest. Detailed surveying of the ion exhaust can be helpful in checking component functioning within the rocket, for example, the ion emission variation from surface ionizers or the beam focusing of the electrostatic accelerators. An even more important use of detailed beam surveys may be found in studies of space charge neutralization, which is a matter of considerable practical and theoretical importance (e.g., ref. 5). For a carefully designed engine, the spreading of the ion beam downstream of the exit of the accelerator is a quantitative measure of the effectiveness of the space charge neutralization (ref. 6). Therefore, detailed maps of the ion beam with and without

electron injection may be used as a measure of beam neutrality under well controlled experimental conditions.

This report describes the design, calibration, and use of a small probe device (0.001 cm in diam.) for measuring beam power at a point and power distribution in high-velocity ion beams. It is called a "hot-wire calorimeter." No other instrument of comparable size is available at this time to measure local ion-beam parameters.

The interception and conversion of ion kinetic energy into heat at a fine-wire surface has been calculated using the classical free-molecule flow analysis, and the dissipation of this heat to the cooled supports is treated as a one-dimensional thermal-conduction problem. The analysis directly relates the voltage output from the hot wire to the local ion-beam power for operation with either constant wire current or constant wire temperature.

Hot-wire calorimeters have been used since February, 1960, in NASA research on ion rockets at the Lewis Research Center. Experimental examples are reported herein of hot-wire measurements in cesium and mercury ion beams with a total current of up to 100 milliamperes that have been accelerated electrostatically to 1 to 20 kilovolts. A detailed description of experimental technique is included with the data presentation.

The probe development is discussed in this report only as it relates to ion rocket research. However, the hot-wire calorimeter could be applied to measurements in any high-energy particle beam.

THEORETICAL ANALYSIS

STEADY-STATE ANALYSIS

Almost any solid surface when placed in a high-energy ion beam has one of the basic ingredients of an ion-beam calorimeter, the ability to convert ion kinetic energy into heat. The design of a useful calorimetric probe also requires: (1) that the sampling cross-sectional area of the surface in the ion beam is known, (2) that the net energy transfer from the ions to the metal surface is known (i.e., the effective accommodation coefficient), and (3) that the heat flow can be metered to give an electrical signal proportional to the ion power intercepted. The first two requirements are common to all calorimeters in ion beams, and the devices can be distinguished by the method used to satisfy the third requirement. Therefore, the following analysis emphasizes the convenient

method that the hot-wire calorimeter uses to give a signal related to the local ion power. This aspect of the problem can be treated in detail because it is straightforward; it involves one-dimensional conduction of heat produced by the ion power, intercepted along the fine wire, to cooled supports at each end. On the other hand, the calculations of the effective cross-sectional area and the ion-surface energy exchange together with the associated problems of sputtering and secondary electron emission are less certain. In the analysis which follows, arguments based on theory are given in support of the assumptions used for the present calculations. Later, preliminary experimental data are presented in the section RESULTS AND DISCUSSION concerning these two assumptions.

Steady-state sensitivity to ion beam.—The problem considered here is the steady operation of a fine wire in a vacuum and in a high-energy ion beam at wire temperatures up to about 600° K. Figure 1 shows the coordinate system which is used. Since the ratio of length to diameter of the

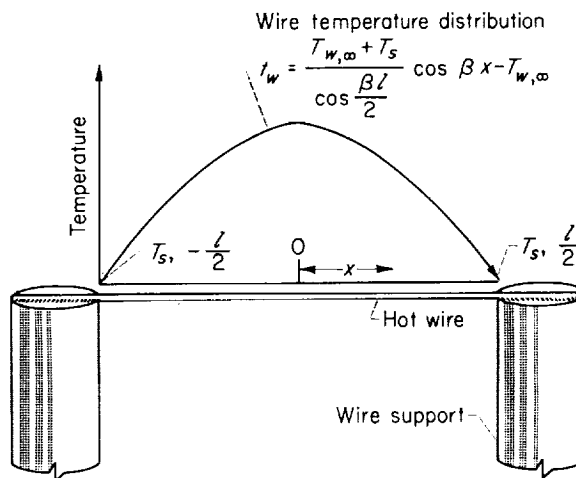


FIGURE 1.—Diagram of hot-wire geometry and temperature distribution.

wire will always be greater than 100, all temperature gradients in the radial and circumferential directions are neglected compared with the axial gradient. That is, the wire metal is assumed to be a uniform temperature at each station x .

The steady-state energy balance for a unit length at any station x along the wire may be written by equating the conduction of heat to the

supports to the sum of joulean heating and beam power addition:

$$q_J + q_B = q_K \quad (1)$$

(All symbols are defined in appendix A.) Equation (1) neglects both the radiant heat loss from the wire and the molecular conduction loss through the surrounding gas. Both of these heat losses may be considered as errors in the hot-wire sensitivity, and both are discussed in detail later in this section.

The quantity q_J is the rate of production of joulean heat due to the detective current I . It is a function of the local resistivity along the wire, which is temperature dependent:

$$\left. \begin{aligned} q_J &= I^2 r \\ r &= \frac{4\sigma}{\pi D^2} [1 + \alpha(t_w - 273)] \end{aligned} \right\} \quad (2)$$

The quantity q_B is the heating rate caused by the conversion of ion kinetic energy into heat at the wire surface. Appendix B treats this aspect of the problem together with the associated problems of sputtering and accommodation coefficient in detail, and the result may be written simply as

$$q_B = a_c D j V \quad (3)$$

For this work, the beam power density jV is assumed constant along the wire length. The efficiency of the energy conversion is expressed by an effective accommodation coefficient a_c , and the sampling cross-sectional area of the wire probe is the geometric section lD . As discussed in appendix B, the accommodation coefficient is expected to be near 1.0, and $a_c = 1.0$ has been used throughout for the present calculations. The effective cross-sectional area should be equal to the actual area lD provided that the wire operates at the local beam potential. However, negligible error is incurred if the wire is operated at a potential relative to the beam, which is small compared with the beam accelerating potential. Other practical considerations mentioned under RESULTS AND DISCUSSION govern the choice of operating potential. The geometric cross section is used in this report, because the ion beams being considered have been accelerated through 1000 to 20,000 volts, whereas the operating potential of the hot-wire probe is usually between 0 and 10 volts relative to ground.

The symbol q_K represents heat loss rate by conduction along the wire to the cooled supports:

$$q_K = -\frac{\pi K D^2}{4} \frac{d^2 t_w}{dx^2} \quad (4)$$

The combination of equations (1) to (4) gives a differential equation expressing the wire temperature as a function of axial position:

$$\frac{d^2 t_w}{dx^2} + \beta^2 t_w = -\beta_1^2 \quad (5)$$

where

$$\begin{aligned} \beta^2 &= \left(\frac{4}{\pi l D^2} \right)^2 \frac{\sigma \alpha}{K} I^2 \\ \beta_1^2 &= \frac{4 a_c j V}{\pi D K} + \left(\frac{4}{\pi l D^2} \right)^2 \frac{\sigma \alpha}{K} I^2 \left(\frac{1}{\alpha} - 273 \right) \end{aligned}$$

The solution of equation (5) is detailed in appendix B using the boundary conditions that the wire temperature is a constant T_s at each support. The resulting equation is

$$t_w = \frac{T_{w,\infty} + T_s}{\cos \frac{\beta l}{2}} \cos \beta x - T_{w,\infty} \quad (6)$$

This is the cosine temperature distribution which is plotted in figure 1. The wire temperature averaged over the length is required to relate the measured wire resistance to the detection current and the beam power input. The average wire temperature is then

$$T_w = \frac{1}{l} \int_{-(l/2)}^{+(l/2)} t_w dx$$

or

$$T_w - T_s = (T_{w,\infty} + T_s) \left[\frac{\tan \frac{\beta l}{2}}{\frac{\beta l}{2}} - 1 \right] \quad (7)$$

To complete the analysis of the hot-wire calorimeter, the average temperature is related to the measured hot-wire voltage drop E by the temperature coefficient of resistivity and Ohm's law:

$$\left. \begin{aligned} E &= IR \\ R &= \frac{4\sigma l}{\pi D^2} [1 + \alpha(T_w - 273)] \end{aligned} \right\} \quad (8)$$

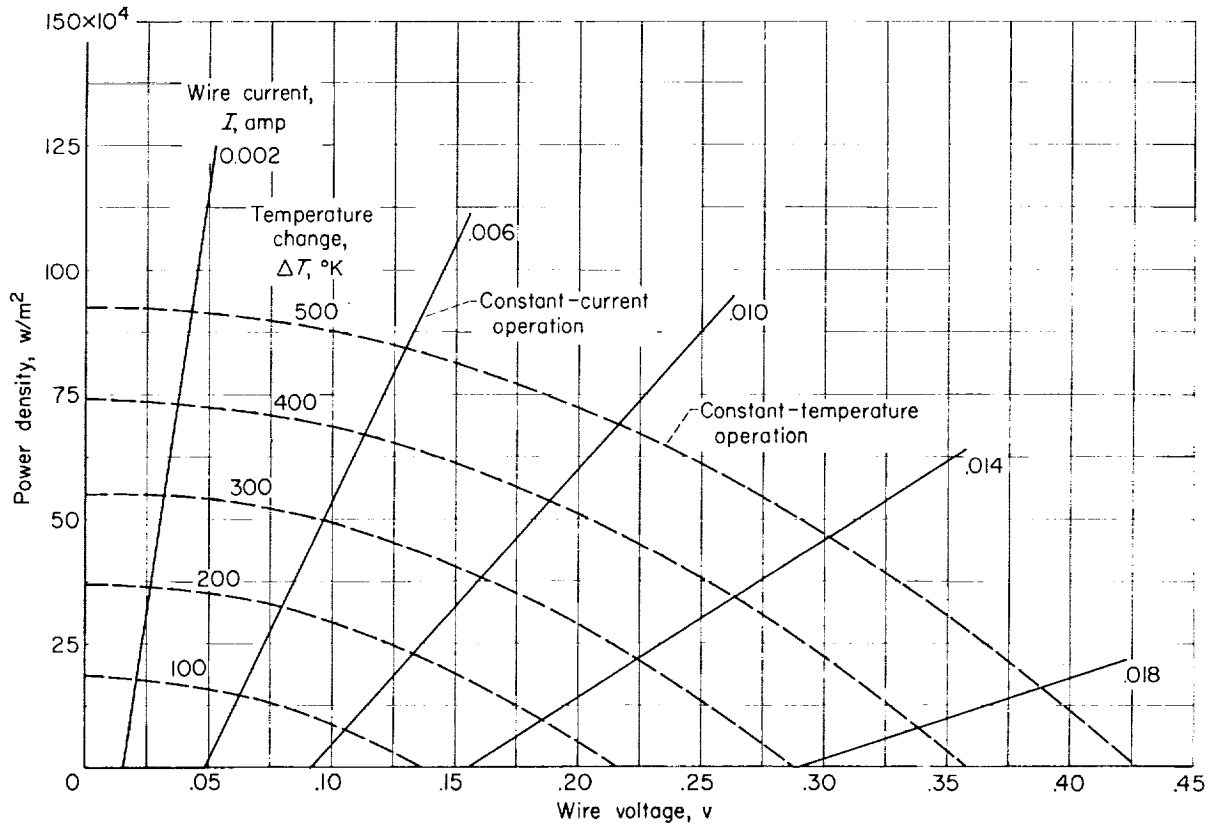


FIGURE 2.—Typical calibration of hot-wire calorimeter. Tungsten wire; diameter, 0.000508 centimeter; length, 0.203 centimeter.

A typical calibration map calculated from equations (7) and (8) is shown in figure 2. Parametric lines of constant wire current and constant wire temperature (or resistance) are plotted, because, as in the hot-wire anemometer familiar in aeronautics, amplifier circuits can be designed conveniently for either constant-temperature or constant-current operation.

Equations (7) and (8) make it possible to select a hot-wire calorimeter that is suitable for operation in the range of beam power densities expected in a specific test. Not only can the operating current or temperature be chosen for a particular operation, but the wire length, diameter, and material can also be chosen from a rather wide selection of commercially available wire. Some examples of this flexibility are shown in figure 3.

The examples in figures 2 and 3 show that the constant-current parametric lines are approximately linear. This suggests that equations (7) and (8) can be simplified for many practical probe designs and operating conditions. By replacing

the tangent of the angle $(\beta l/2)$ in equation (7) by the first two terms of a power series, as discussed in appendix B, equations (7) and (8) may be reduced to the following:

$$E = \left(\frac{I}{C}\right) jV + B \quad \left(\frac{\beta l}{2} < 9^\circ\right) \quad (9)$$

where

$$\frac{1}{C} = \frac{4a_c \sigma \alpha}{3\pi^2 K} \left(\frac{l}{D}\right)^3$$

$$B = IR_s + \frac{IR_s}{a_c l DC} I^2$$

Equation (9) deviates from the exact equation by less than 1 percent if $\beta l/2$ is less than 9° . Therefore, the constant-current sensitivity of a hot-wire calorimeter may be readily calculated as

$$\left. \frac{\Delta(jV)}{\Delta E} \right|_{I=\text{Constant}} = \frac{C}{I} = \frac{3\pi^2 K}{4a_c \sigma \alpha} \left(\frac{D}{l}\right)^3 \frac{1}{I} \quad \left(\frac{w}{(\text{sq m})(v)} \right) \quad (10)$$

Equation (10) emphasizes the need for accurate measurements of wire length and diameter and for knowledge of three wire physical properties: thermal conductivity K , electrical resistivity σ , and temperature coefficient of resistance α . Fortunately, in practice it is not necessary to have independent physical constants as accurate as an error analysis of equation (10) would imply. A

simple empirical calibration for C can be made when the probe is out of the ion beam and in the high vacuum of the test facility. That is, it is convenient to use equation (9) for the case of zero beam power density for a direct comparison of theory with experiment. Equation (9) for $jV=0$ can be arranged as follows:

$$\frac{R}{R_s} = 1 + \left(\frac{1}{a_c D l C} \right) I^2 \quad (11)$$

The experimental calibration for C may be readily calculated from the measured slope of a plot of R/R_s against I^2 , because D and l can be measured independently and a_c is assumed to be 1.0. This calibration serves as a routine check of the physical properties used in the calculations. The procedure is discussed in detail later.

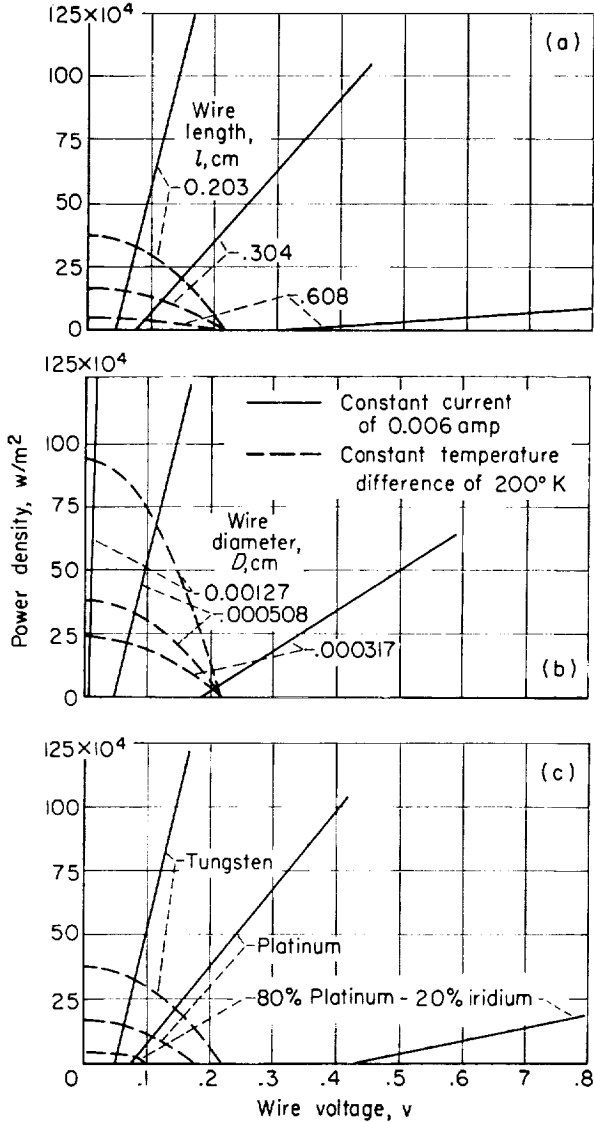
To summarize briefly, equations (7) and (8) are analytically exact solutions to the hot-wire-calorimeter sensitivity in a high-energy ion beam. A simplified solution, which is accurate to within 1 percent in a practical range of parameters, is also presented as equation (9). Using equation (9), the hot-wire sensitivity to the ion beam for constant-wire-current operation is related to an experimental calibration curve which can be easily obtained from the hot wire while it is out of the ion beam in a high vacuum. To conclude the analysis, the following paragraphs consider the errors involved in the preceding analysis because it (1) neglected molecular conduction of heat through the rarefied air of the vacuum facility, and (2) neglected thermal radiation loss from the wire.

Molecular conduction error.—The power balance for an element of wire losing heat to the surrounding rarefied air of the high-vacuum facility and to the wire supports may be written as

$$q_B + q_J = q_K + q_{FM} \quad (12)$$

q_B , q_J , and q_K are given by equations (2), (3), and (4). The heat loss through the ambient air q_{FM} can be obtained from a molecular conduction analysis (e.g., ref. 7) which relates the heat transfer to the air pressure:

$$\left. \begin{aligned} q_{FM} &= h \pi D (t_w - T_a) \\ h &= \left(\frac{3a_c}{2} \right) \sqrt{\frac{2\mathcal{R}}{\pi M_a T_a}} \frac{p}{0.987 \times 10^{-5}} \end{aligned} \right\} \quad (13)$$



(a) Wire length. Tungsten wire; diameter, 0.000508 centimeter.
 (b) Wire diameter. Tungsten wire; length, 0.203 centimeter.
 (c) Wire material. Wire diameter, 0.000508 centimeter; length, 0.203 centimeter.

FIGURE 3.—Variables affecting wire calibration.

where 0.987×10^{-5} is a conversion factor from atmospheres to newtons per square meter. Combining equations (2), (3), (4), (12), and (13) gives the following differential equation:

$$\frac{d^2 t_w}{dx^2} - \eta^2 t_w = -\eta^2 t_s \quad (14)$$

The solution is analogous to that outlined earlier for equation (5), except that the temperature distribution along the wire follows a hyperbolic cosine law given by equation (15). The air temperature T_a is assumed to be equal to the support temperature T_s for numerical simplicity. Similarly, the length average temperature is analogous to equation (7), and it is given here as equation (16):

$$t_w - T_s = (T_{w,\infty}^* - T_s) \left(1 - \frac{\cosh \frac{\eta x}{2}}{\cosh \frac{\eta l}{2}} \right) \quad (15)$$

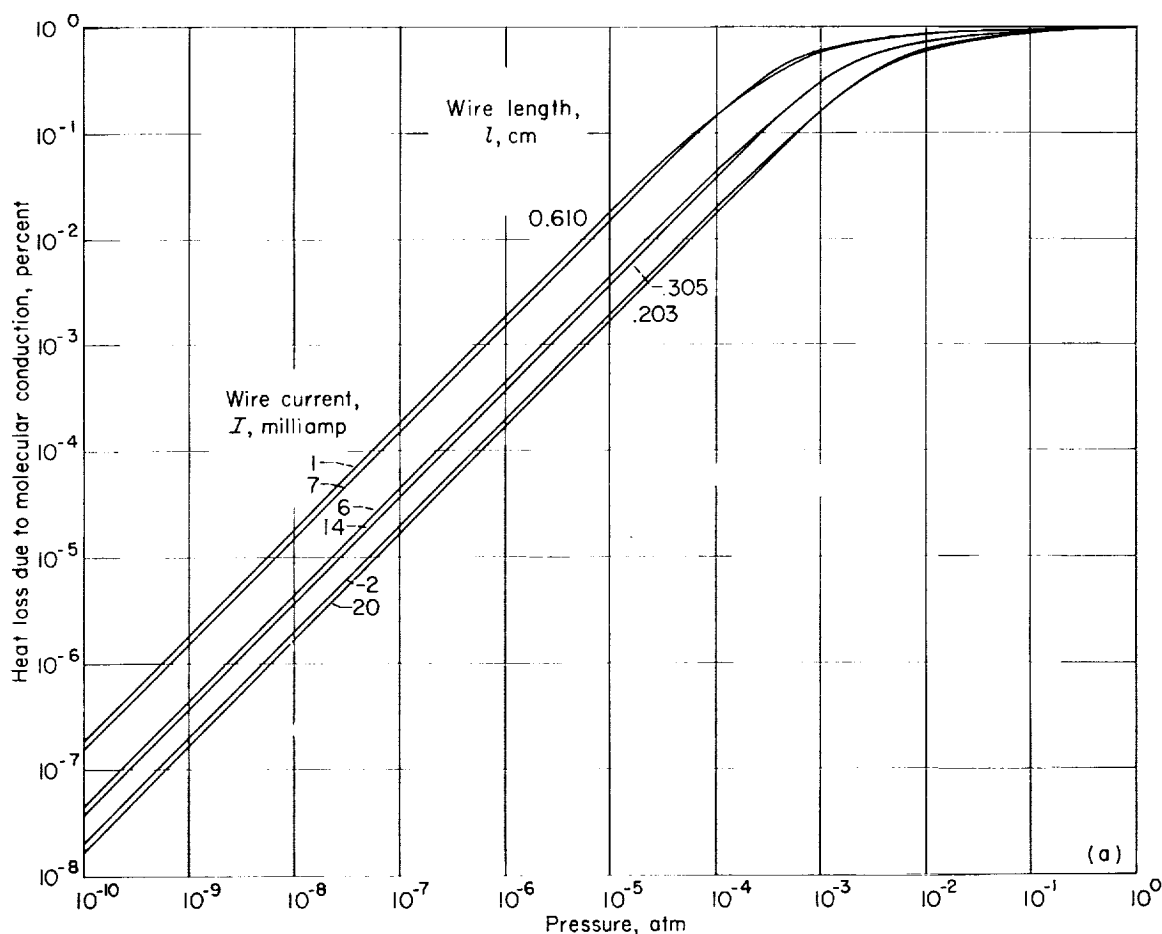
$$T_w - T_s = (T_{w,\infty}^* - T_s) \left(1 - \frac{\tanh \frac{\eta l}{2}}{\frac{\eta l}{2}} \right) \quad (16)$$

By writing the energy balance (eq. (12)) for the entire wire and by using equations (15) and (16), the ratio Φ of the heat lost by conduction to the supports to the heat lost by molecular conduction to the air can be found:

$$\Phi = \frac{Q_K}{Q_{FM}} = \left(\frac{K}{hD} \right) \left(\frac{D}{l} \right)^2 \left(\frac{T_{w,\infty}^* - T_s}{T_w - T_s} \right) \frac{\eta l}{2} \tanh \frac{\eta l}{2} \quad (17)$$

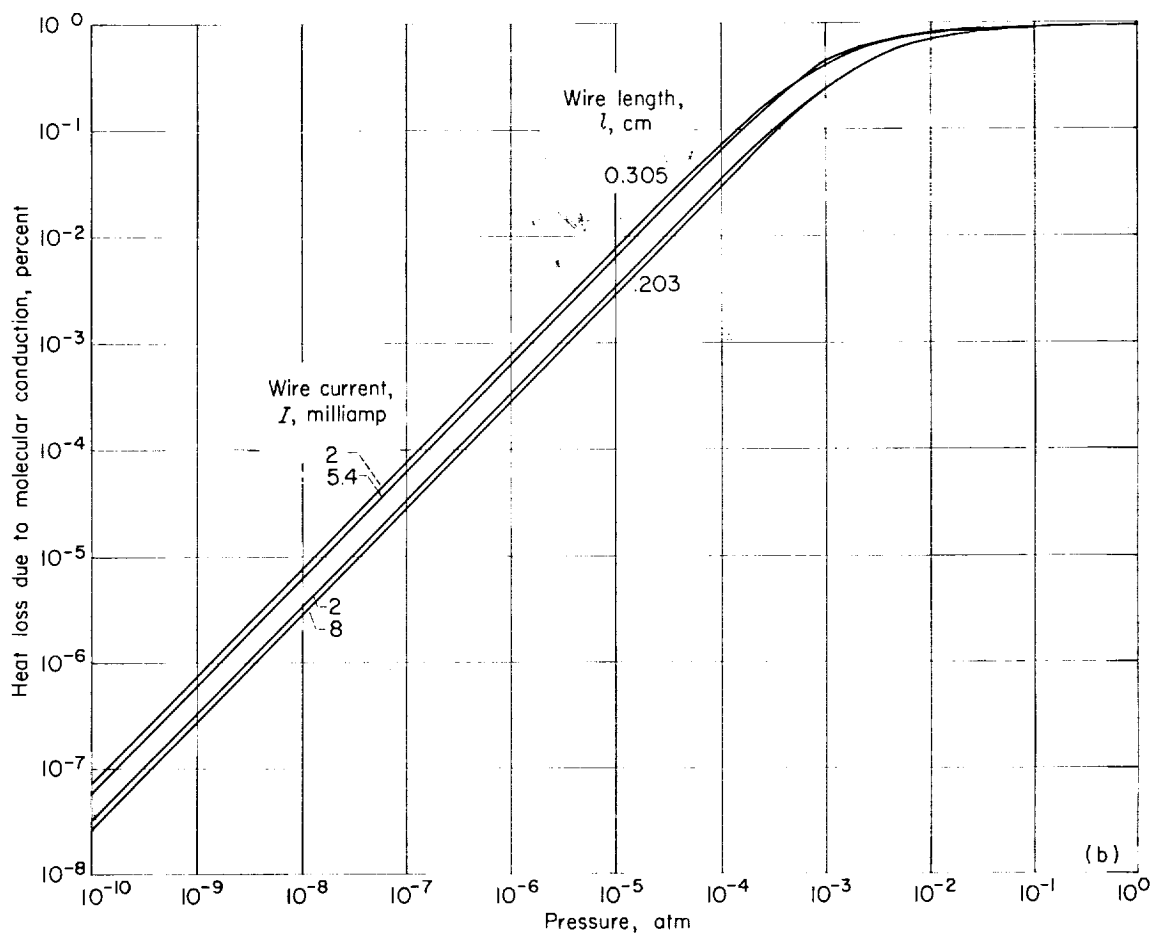
The error δ_{FM} caused by neglecting molecular conduction in the hot-wire-calorimeter analysis is the ratio of the heat lost by molecular conduction to the total heat loss:

$$\delta_{FM} = \frac{Q_{FM}}{Q_J + Q_H} = \frac{1}{1 + \Phi} \quad (18)$$



(a) Tungsten wire; diameter, 0.000508 centimeter.

FIGURE 4.—Molecular conduction error as function of air pressure.



(b) Tungsten wire; diameter, 0.000317 centimeter.

FIGURE 4.—Continued. Molecular conduction error as function of air pressure.

For a specific wire and operating condition, the error δ_{FM} is a function only of the pressure in the vacuum facility. Figure 4 was calculated from equations (13), (17), and (18); this figure shows δ_{FM} for typical example wires and operating conditions assuming that the vacuum atmosphere is air. Hot-wire-calorimeter application to ion rocket research should always be in test facilities operating below 10^{-7} atmosphere (refs. 2 and 3). Figure 4 shows that negligible error (<0.01 percent) was incurred in the hot-wire-calorimeter analysis because molecular conduction was assumed to be zero.

Thermal radiation error.—On the other hand, the radiant heat loss from a fine wire in a vacuum may be expected to become the dominant heat loss as the wire temperature is increased. Con-

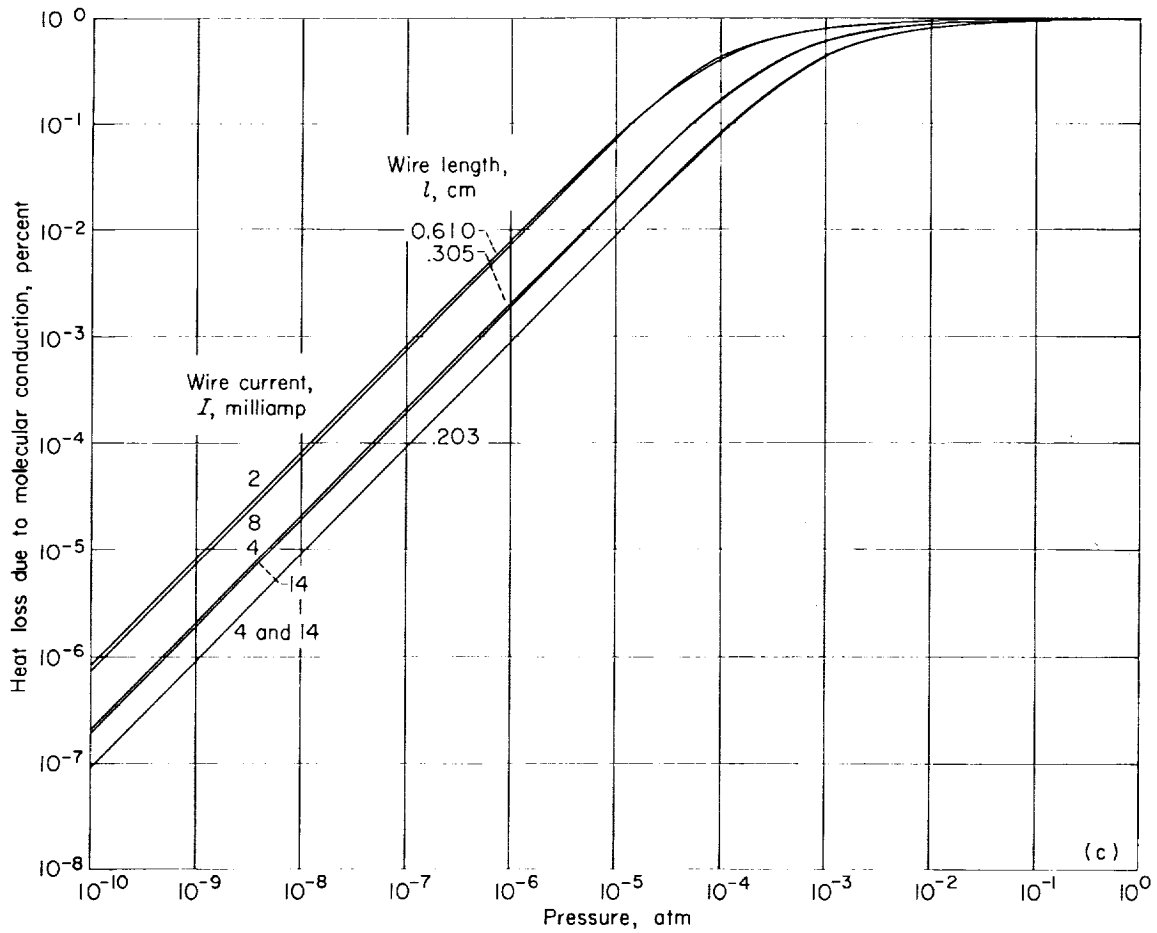
sider the energy balance on an element of hot wire which is losing heat by conduction to the supports and by thermal radiation

$$q_B + q_U = q_K + q_R \quad (19)$$

This problem cannot be solved analytically as equations (1) and (12) can be, because the differential equation is nonlinear in t_w ; that is,

$$\frac{d^2 t_w}{dx^2} - \beta_2^2 t_w^4 + \beta^2 t_w = -\beta_1^2 \quad (20)$$

However, by restricting interest to the case where radiation is small compared with the total heat loss, an approximate solution may be found. When $q_R < 0.1 q_K$, the temperature distribution along the wire is given approximately by equation



(c) 80-Percent-platinum—20-percent-iridium wire; diameter, 0.00101 centimeter.

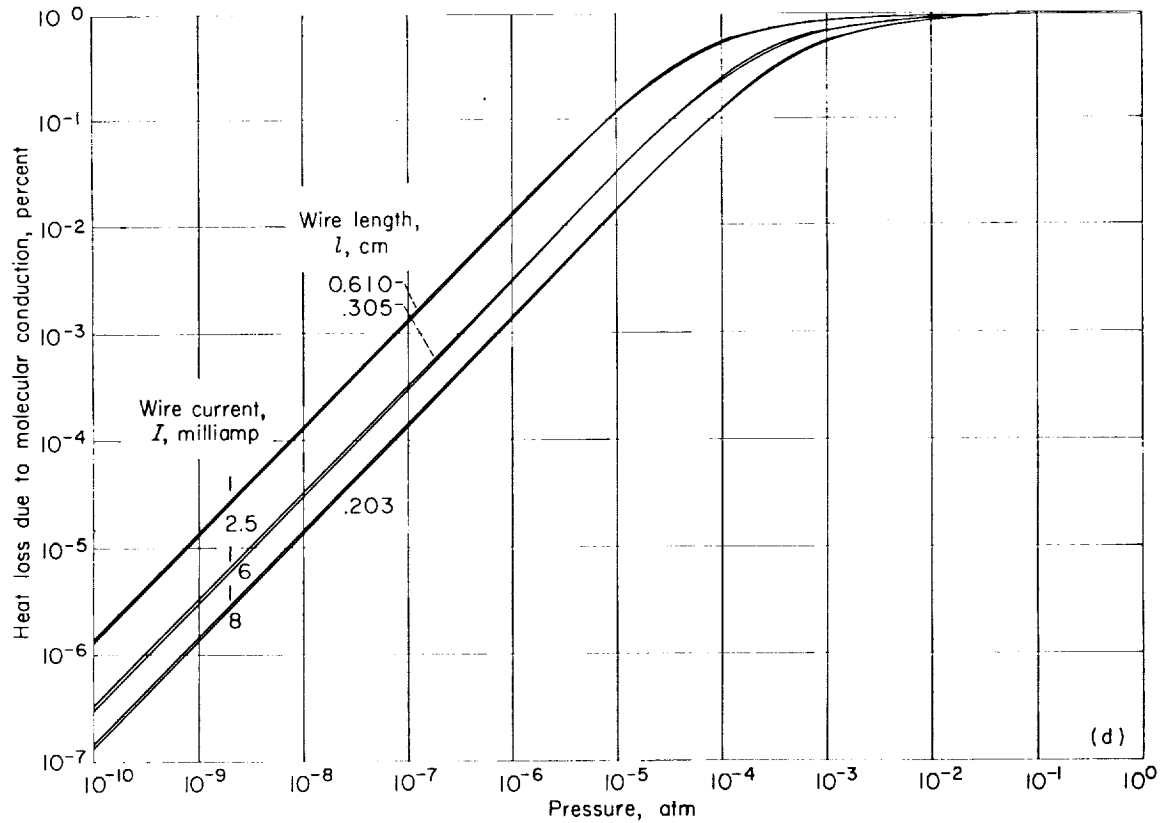
FIGURE 4.—Continued. Molecular conduction error as function of air pressure.

(6). The radiant heat loss may be estimated then by substituting equation (6) into equation (21) to obtain

$$Q_R \approx \epsilon \sigma_{SB} \pi D \left(\int_{-(1/2)}^{+(1/2)} t_w^4 dx - T_s^4 l \right) \quad (21)$$

Equation (22) is the result of the integration.

$$Q_R \approx \frac{\epsilon \sigma_{SB} \pi D}{\beta} \left\{ \frac{3}{4} (T_{w, \infty} + T_s)^4 \frac{\frac{\beta l}{2}}{\cos^4 \frac{\beta l}{2}} + \left[\frac{3}{4} (T_{w, \infty} + T_s)^4 - 8 (T_{w, \infty} + T_s)^3 T_{w, \infty} \right] \frac{\tan \frac{\beta l}{2}}{\cos^2 \frac{\beta l}{2}} \right. \\ \left. + \left[\frac{1}{2} (T_{w, \infty} + T_s)^4 + 6 (T_{w, \infty} + T_s)^2 T_{w, \infty}^2 - 8 (T_{w, \infty} + T_s) T_{w, \infty}^3 \right] \tan \frac{\beta l}{2} \right. \\ \left. + \frac{8}{3} (T_{w, \infty} + T_s)^3 T_{w, \infty} \tan^3 \frac{\beta l}{2} + 6 (T_{w, \infty} + T_s)^2 T_{w, \infty}^2 \frac{\frac{\beta l}{2}}{\cos^2 \frac{\beta l}{2}} + 2 (T_{w, \infty}^4 - T_s^4) \left(\frac{\beta l}{2} \right) \right\} \quad (22)$$



(d) 80-Percent-platinum—20-percent-iridium wire; diameter, 0.000635 centimeter.

FIGURE 4.—Concluded. Molecular conduction error as function of air pressure.

The error δ_R caused by neglecting radiant heat loss in the hot-wire-calorimeter analysis is the ratio of the radiant heat loss to the total heat loss (approximated here by the conduction heat loss Q_K because $Q_R < 0.1 Q_K$ is assumed in eq. (19)):

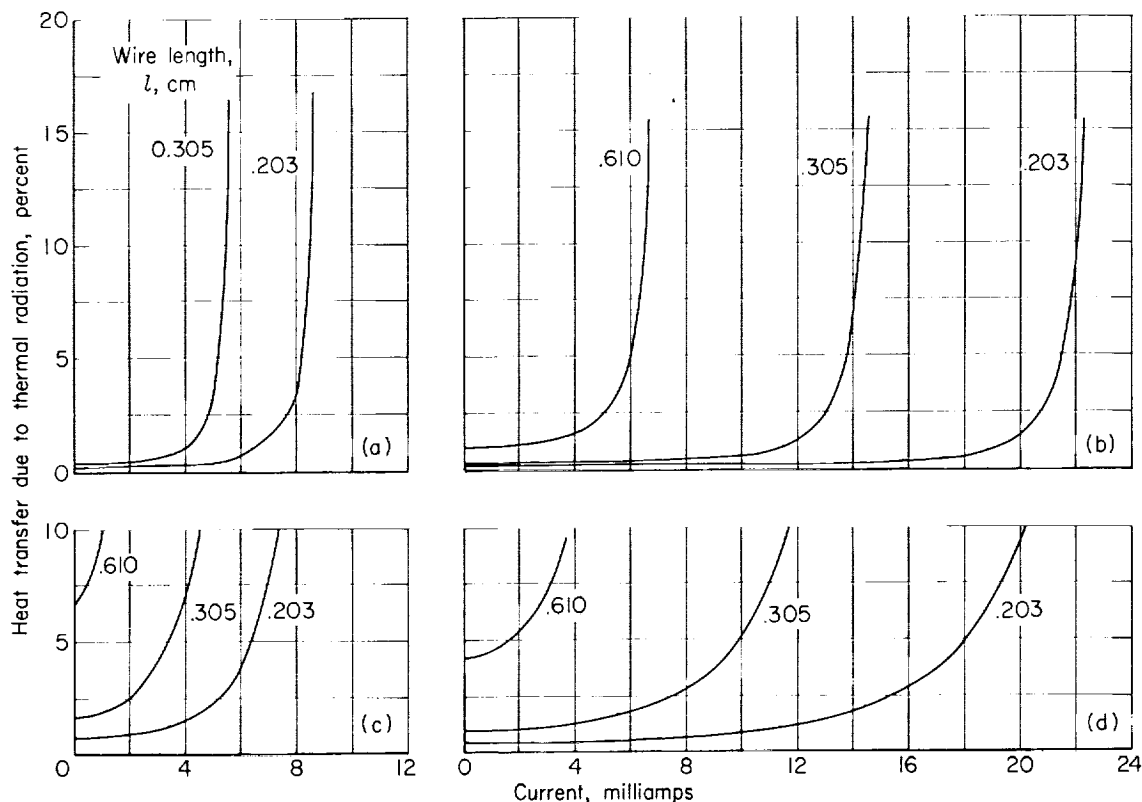
$$\delta_R \equiv \frac{Q_R}{Q_B + Q_J} \approx \frac{Q_R}{Q_K} \quad (23)$$

For a specific wire, the error δ_R is a function only of the operating current I (i.e., operating temperature). Figure 5 was calculated from equations (7), (8), and (22) for typical example wires. For simplicity, gray-body emissivity or a total emissivity of 0.10, independent of temperature, was assumed in these calculations. Reference 8 lists the total emissivity for tungsten (p. 141) and platinum (p. 104) (or iridium, p. 73) wires as less than 0.07 at 600° K. For these approximate error calculations, the value of 0.10 was considered to be realistic and conservative.

One of the most interesting characteristics of δ_R shown in figure 5 is the zero-current value of δ_R . Although both Q_R and Q_K approach zero as the wire current goes to zero, the limiting value of the ratio δ_R is finite and given by the following equation:

$$\lim_{I \rightarrow 0} \delta_R = \frac{4}{3} \frac{\sigma_{SB} \epsilon l^2}{K D} T_i^3 \quad (24)$$

For simplicity, it is desirable to design a probe and to choose an operating current so that δ_R is negligible (< 0.01) over the expected range of beam power inputs. Equation (24) suggests that the wire length is probably the primary variable to be controlled in designing for minimum radiation error. Therefore, although the radiation error analysis is approximate, it is probably sufficient for design purposes. The exact magnitude of the thermal radiation error may be determined best by an empirical calibration, as discussed in the section RESULTS AND DISCUSSION.



(a) Tungsten wire; diameter, 0.000317 centimeter.
 (b) Tungsten wire; diameter, 0.000508 centimeter.
 (c) 80-Percent-platinum-20-percent-iridium wire; diameter, 0.000635 centimeter.
 (d) 80-Percent-platinum-20-percent-iridium wire; diameter, 0.001016 centimeter.

FIGURE 5.—Estimate of heat loss from hot wires due to thermal radiation.

TRANSIENT ANALYSIS

The primary application of hot-wire calorimeters to present ion rocket research is in steady-state operation, in which mean voltage output is related to time-averaged beam power density. Even for these applications, however, the response rate of the hot wire may be important to ensure that the sweep of the probe through the beam is slow enough for steady-state sensitivity to apply. Furthermore, future research may find the transient response of the hot wires useful for studying low-frequency (e.g., 0 to 10,000 cps) beam power fluctuations.

The energy balance for the transient case can be written as follows:

$$q_s = q_J + q_B - q_K \quad (25)$$

$$T_w - T_s = (T_{w,\infty} + T_s) \left[\frac{\tan \frac{\beta l}{2}}{\frac{\beta l}{2}} - 1 + \sum_{n=0}^{\infty} 2 \left(\frac{2}{\lambda_n l} \right)^2 \left(\frac{\lambda_n^2}{\beta^2 - \lambda_n^2} - \frac{\lambda_n^2}{\beta_0^2 - \lambda_n^2} \right) e^{-\left(\frac{\lambda_n^2}{\beta^2} - 1 \right) \frac{t}{\tau}} \right] \quad (28)$$

The rate of heat storage q_s is given by

$$q_s = \frac{\pi D^2}{4} \rho c \frac{\partial t_w}{\partial t} \quad (26)$$

Combining equations (2), (3), (4), and (26) leads to the following partial differential equation:

$$\frac{\rho c}{K} \frac{\partial t_w}{\partial t} = \frac{\partial^2 t_w}{\partial x^2} + \beta^2 t_w + \beta_1^2 \quad (27)$$

The solution of equation (27) is given in detail in appendix B for a step change in wire current from I_0 to I . The initial condition used for the solution is that the wire is operating at a steady-state current I_0 before the step change; the same boundary conditions are used here as in the solution of equation (5). The resulting equation for the length-average wire temperature is

The time-dependent series converges very rapidly, and a good approximation may be obtained from the first term ($n=0$) alone:

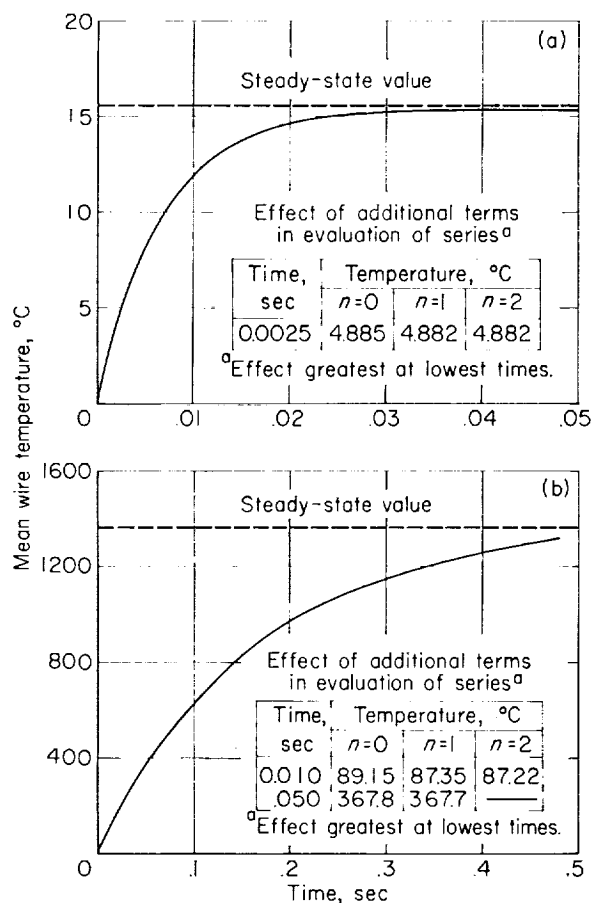
$$T_w - T_s \approx (T_{w, \infty} + T_s) \left\{ \frac{\tan \frac{\beta l}{2}}{\frac{\beta l}{2}} - 1 + \frac{8}{\pi^2} \left[\frac{1}{\left(\frac{\beta l}{\pi}\right)^2 - 1} - \frac{1}{\left(\frac{\beta_0 l}{\pi}\right)^2 - 1} \right] e^{-\frac{t}{\tau_E}} \right\} \quad (29)$$

where

$$\tau_E = \left[\left(\frac{\pi}{\beta l} \right)^2 - 1 \right]^{-1} \tau$$

A sample calculation is given in figure 6. The approximate solution represents the response to within 3 percent for all $t > 0.1 \tau_E$. Equation (29) is the exponential response of a first-order system, so the dynamic characteristics are completely specified by the single time constant τ_E . In general, τ_E depends not only on the wire physical proper-

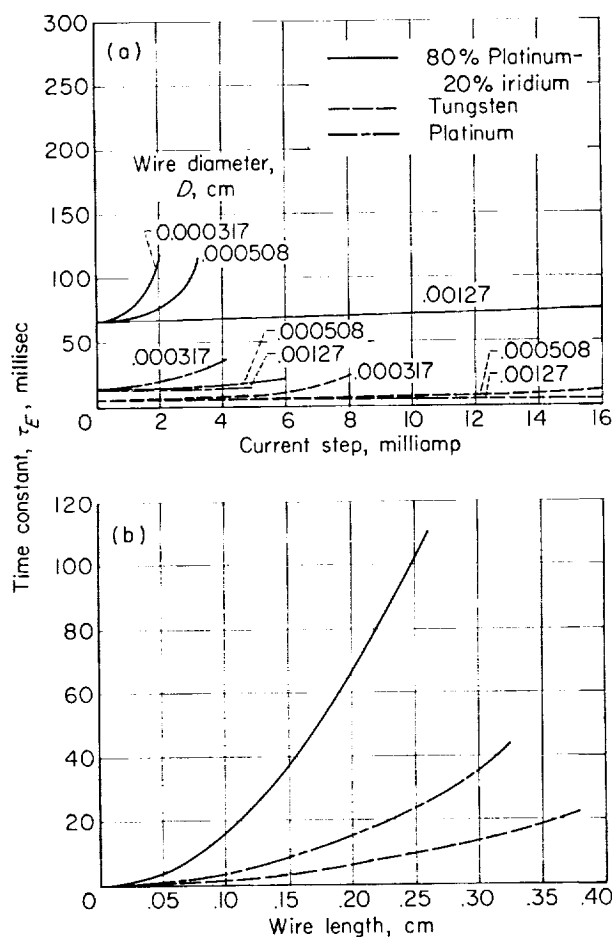
ties and dimensions but also on the steady-state operating current (or temperature). Figure 7(a) shows the effect of wire current and diameter on the time constant with some sample calculations for a specified length of platinum, 80-percent-platinum-20-percent-iridium, and tungsten wires.



(a) Tungsten wire.

(b) 80-Percent-platinum—20-percent-iridium wire.

FIGURE 6.—Mean wire temperature increase with time for current step increase of 0.006 ampere.



(a) Current step size. Wire length, 0.203 centimeter.

(b) Wire length. Constant current.

FIGURE 7.—Effect of various parameters on wire response time.

Note that the predicted time constant at $I=0$ is independent of wire diameter. Furthermore, the time constant at zero current is a good first estimate of the actual time constant of a wire operating at low current. The time constant at zero current is therefore very useful for engineering estimates because of its simplicity:

$$\tau_E|_{I=0} = \left(\frac{\rho c}{K}\right) \frac{l^2}{\pi^2} \quad (30)$$

Equation (30) is plotted in figure 7(b) for several materials over a range of wire lengths.

The choice of a probe for transient measurements may be governed by different desired operating characteristics from probes for steady-state application. However, by working with equations (10) and (30), it should be possible to make good estimates of probe designs which have suitable characteristics for a given application. The design of practical hot-wire-calorimeter probes should consider not only the preliminary design calculations using these equations but also the background of experimental experience which is discussed in the remainder of the text.

EXPERIMENTAL APPARATUS AND PROCEDURE

APPARATUS

High-energy ion sources.—Several types of ion engines are now in operation at the Lewis Research Center. Most of the experience to be reported herein was obtained in the exhaust of engine A, which is a modified version of the engine reported in reference 4. A composite picture of the disassembled engine is shown in figure 8. Cesium metal is contained in a vaporizer behind the round orifice plate on the right in figure 8. The cesium vaporizes and passes through the small holes which can be seen on the plate. The cesium vapor comes in contact with the ionizer which is composed of hot tungsten strips. The tungsten strips are in the square structure in front of the vaporizer plate in figure 8. The cesium atoms are ionized at the surface of the tungsten strips. The cesium ions thus formed are then accelerated by an electrostatic potential maintained on the first electrode directly in front of the ionizer. The second electrode on the far left side is maintained at ground potential as shown on the schematic diagram in the lower portion of figure 8. The first electrode is usually operated at a negative potential with

respect to ground ("accelerate-decelerate" curve). Some data are reported for "accelerate-only" operation; for this mode, the first electrode is also operated at ground potential.

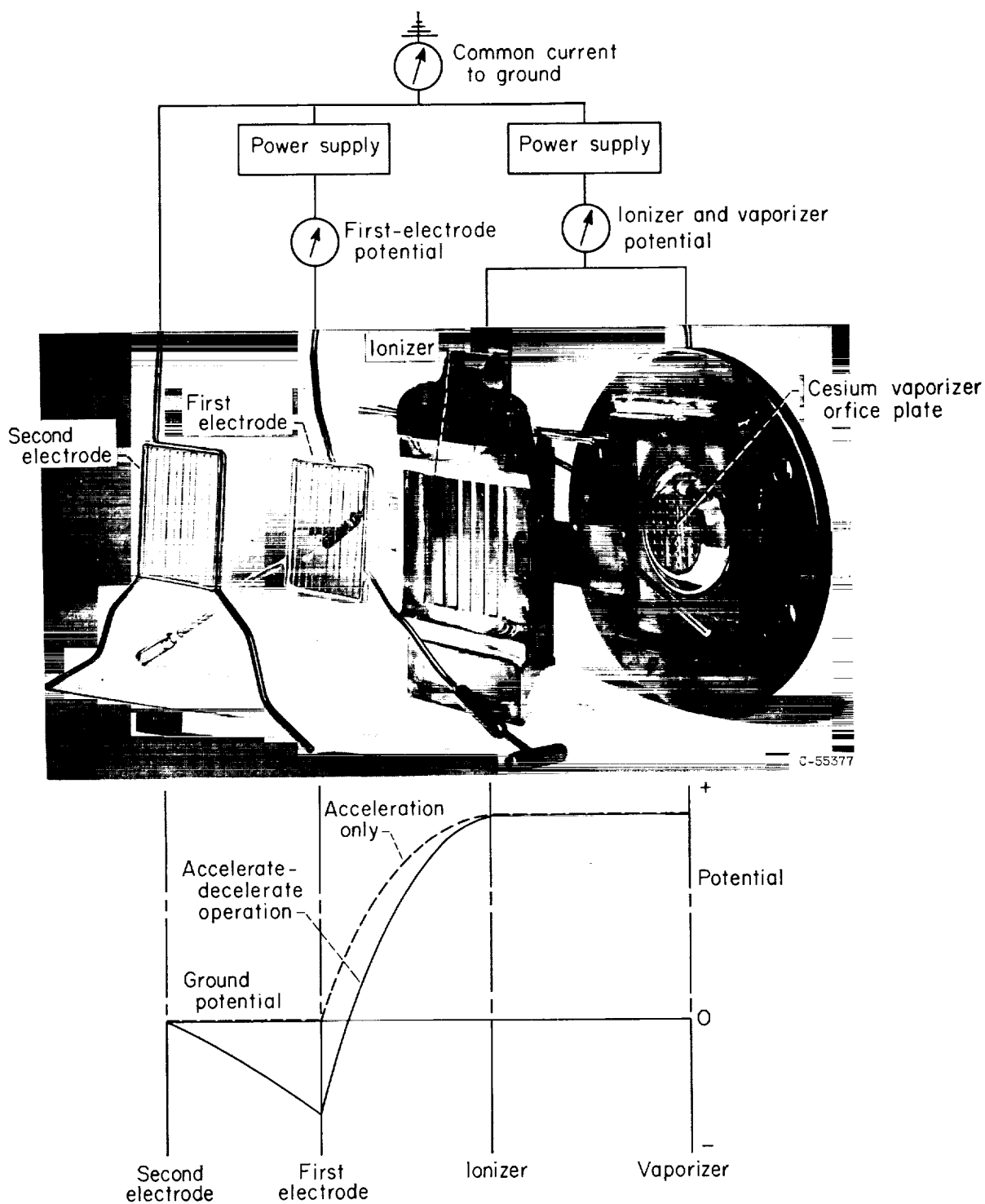
The schematic diagram in the upper portion of figure 8 shows the location of the high-voltage power supplies, together with the potential and current meters for monitoring the ion-beam power.

Other ion engines from which sample surveys are shown in this report are listed in the following table, where the letter designation used for convenience in this text is also given:

Engine	Element ionized	Ionizer	Accelerator	Reference
A	Cesium	Forward vapor feed on tungsten strips	Grid wires	4
B	Cesium	Reverse vapor feed on tungsten plate	Grid wires	9
C	Cesium	Forward vapor feed on tungsten strips	Pierce electrodes	4
D	Cesium	Porous tungsten	Pierce electrodes	-----
E	Mercury	Electron bombardment	Grid wires	10

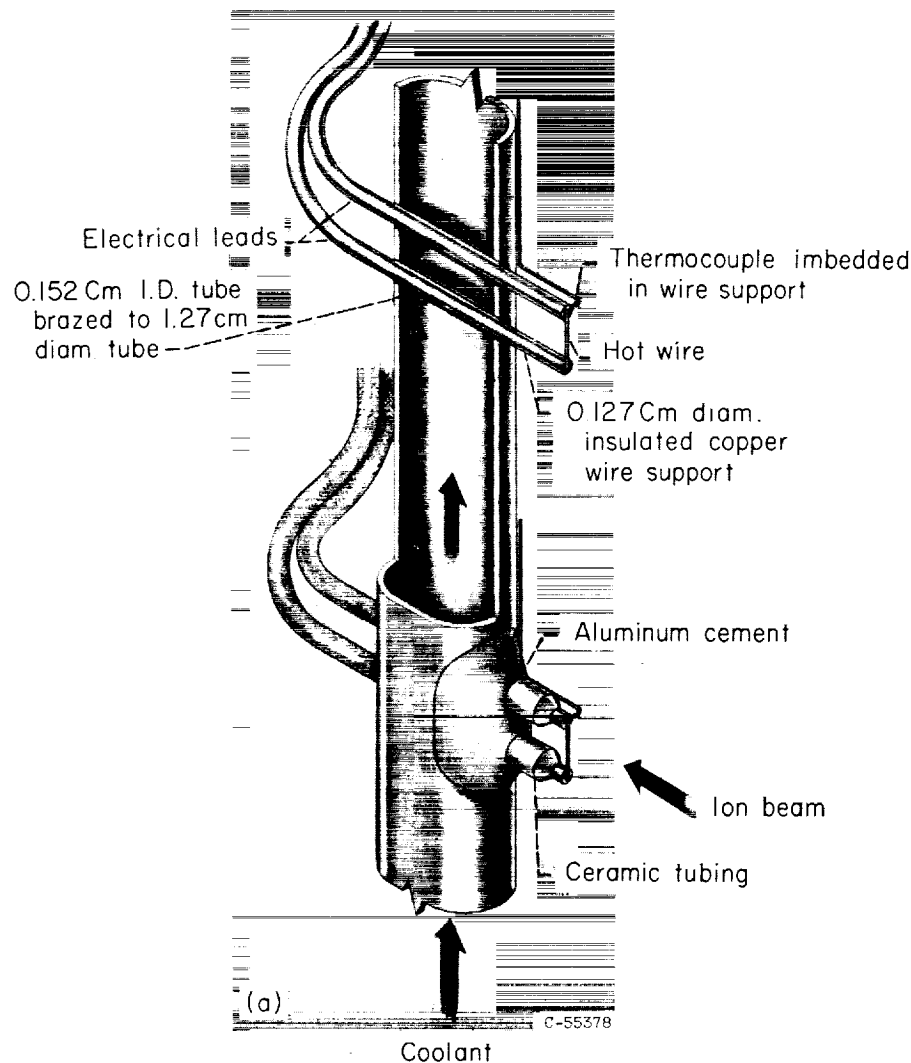
Hot-wire probe.—The probes employed to check the theoretical principles of the previous section are shown in figure 9. The probes are water-cooled and electrically insulated from ground. A schematic diagram of the probe construction is shown in figure 9(a). A 1.27-centimeter-diameter copper tube which was flattened into an elliptical section served as the case for a series of hot-wire elements. Water flowed through the case to cool the hot-wire supports. A detailed sketch of the support construction is also shown in figure 9(a). To ensure that the water case and wire supports were vacuum tight, a 0.152-centimeter tube was inserted through and brazed to the case and a 0.127-centimeter copper support wire was inserted as shown. The support wire was varnish-insulated, and it was surrounded with aluminum cement for good thermal contact with the case. The supports projected about 1.3 centimeters from the case on the side exposed to the ion beam. An iron-constantan thermocouple was silver-soldered to the tip of one of these support pairs. The fine-wire sensitive element was soft-soldered across the supports as shown in figure 9(a).

The present probes have proven adequate for measurements within the ion beams, but they do not represent the end product of a development program. For example, the probe case could be made of an electrical insulating material, such as glass. Since the nonconducting case could not



Plot of potential variation within engine

FIGURE 8.—Details of ion engine A.



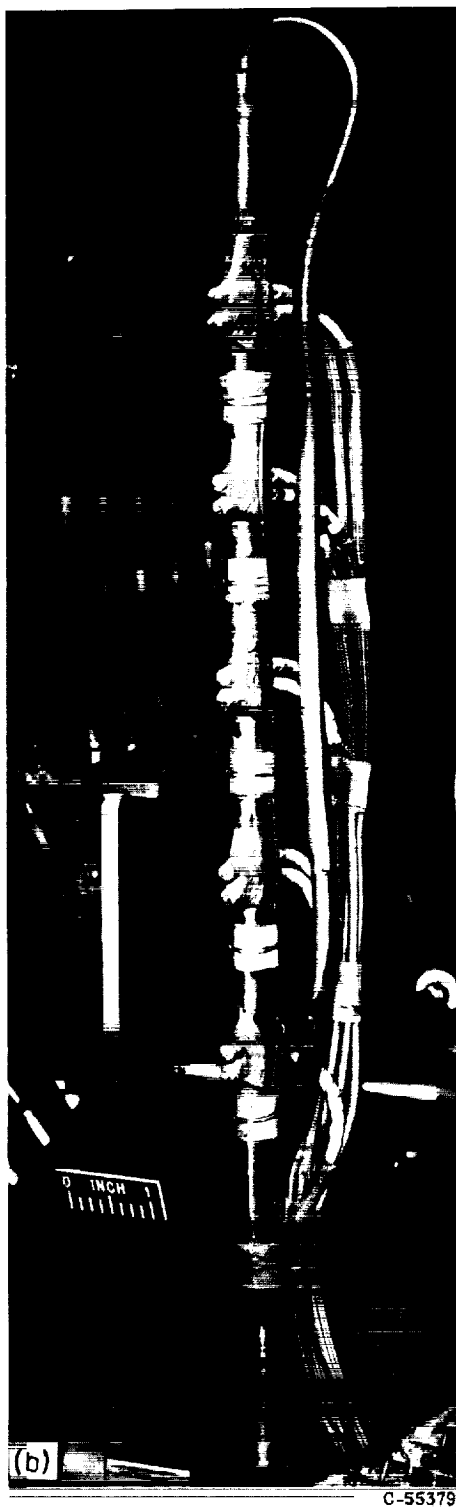
(a) Rake construction.

FIGURE 9.—Hot-wire probes.

act as a direct-current electron source, such a hot-wire rake would be more useful in beam neutralization experiments. Furthermore, the effect of support size and length as well as other effects such as outgassing have not as yet been evaluated. One problem which arose early in the testing was that the wire supports exposed to the beam must be symmetrical in area. This requirement arises from the secondary electron emission characteristics of surfaces in ion beams and is discussed more fully in appendix C.

Survey mechanism.—Because of the lack of symmetry of the ion beams surveyed, it is necessary to survey the entire beam. To minimize the

length of time any one wire is in the ion beam, hot-wire-calorimeter rakes are employed. Thus, not one but as many as five wires are operated in the beam at once. Two different types of actuators were employed in the surveys of engine A. A traversing screw actuator was mounted 46 centimeters downstream of the exit of engine A. This traversing actuator surveyed horizontally across the beam. This particular probe arrangement is shown in figure 9(b). It required about 3 minutes for the actuator to traverse the beam. A copper plate was installed on one side of the screen, so that the probe could be moved into its shadow when not in use. The copper shield served as a

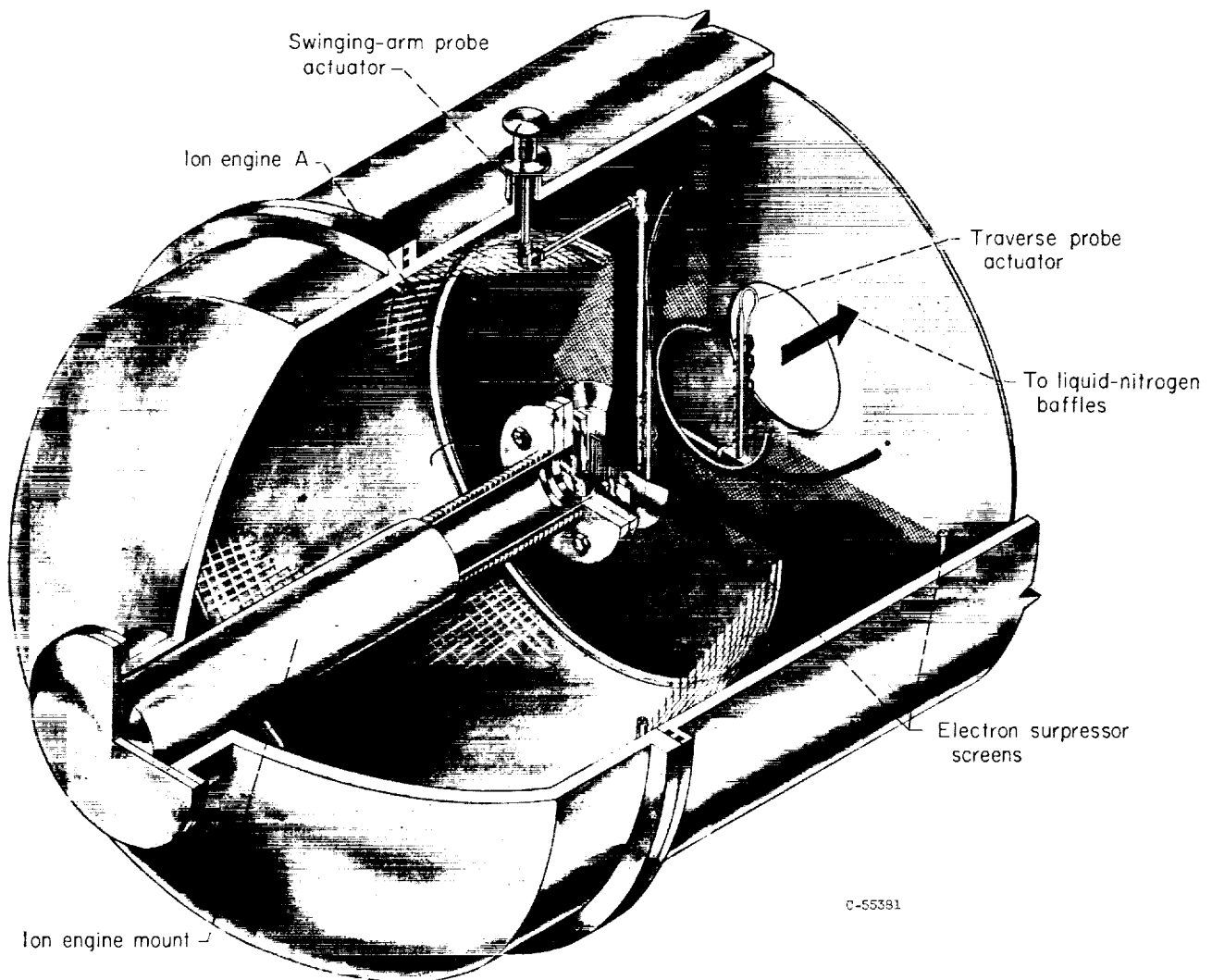


(b) Hot-wire rake on traverse actuator.



(c) Hot-wire rake on swinging arm.

FIGURE 9.--Concluded. Hot-wire probes.



(a) Probe installation in tank.

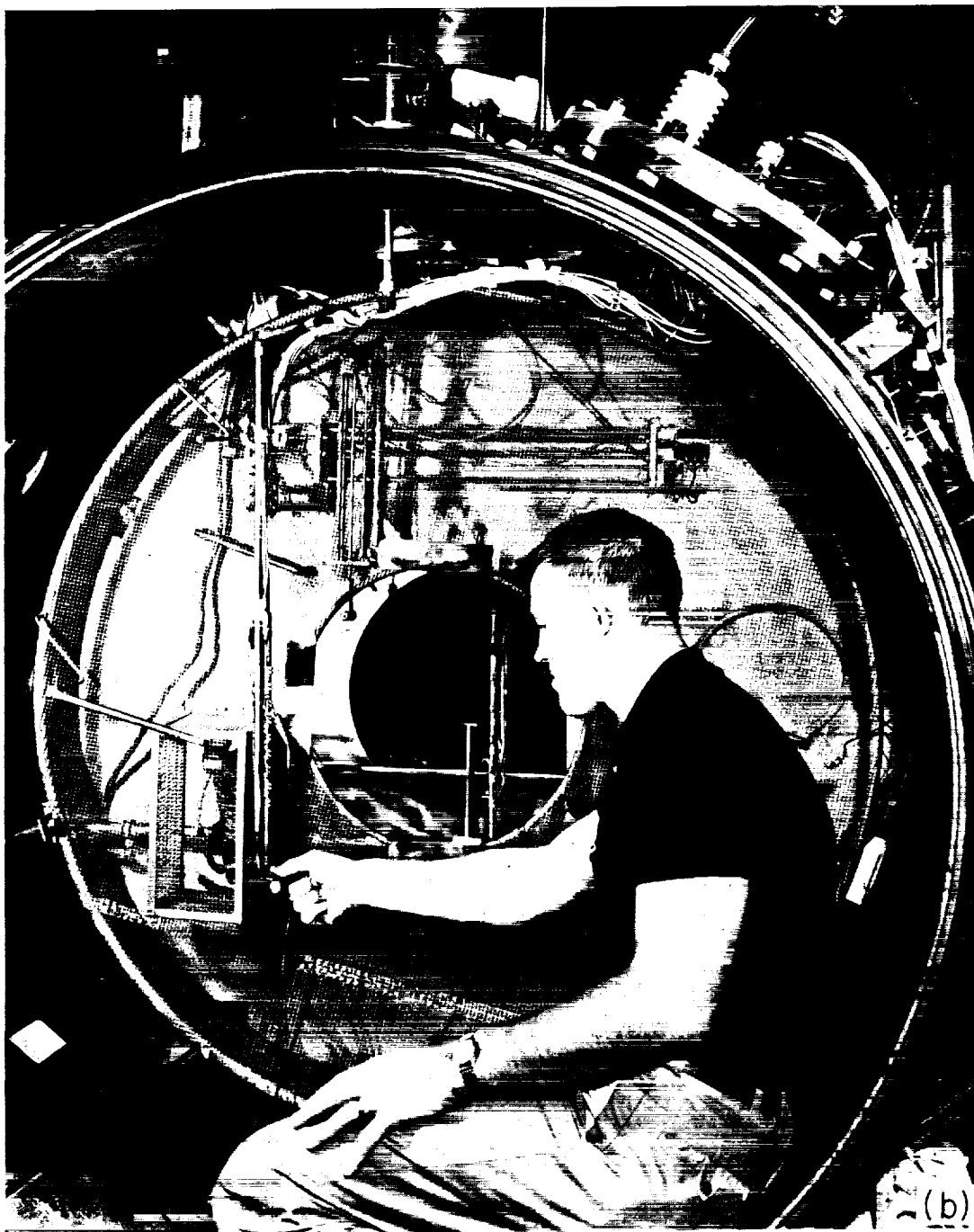
FIGURE 10.--Test facility.

means of protecting the wires against excessive sputtering and also established a definite zero point for wire output.

It was quickly apparent that the complete ion beam was seldom contained within the 45-centimeter hole in the screen. Moreover the time of travel was far slower than necessary for the wire response time, and this caused excessive uncertainty due to a temperature rise of the probe support. These problems were overcome by using a swinging-arm actuator. This actuator is shown in figure 9(c). For this actuator a commercially available grease-sealed vacuum fitting is used on the vacuum tank wall. Through this fitting it is possible to make vertical and rotational

movements of a rod. On the inside of the tank a rigid arm is mounted to the rod from the vacuum fitting. The probe is then mounted on the arm. Rotating the rod thus swings the probe in an arc through the ion beam. For engine A, 30 seconds were used for a full sweep. In each of the other tanks and engines surveyed, only swinging-arm actuators were used.

Test facilities.—A typical vacuum tank facility in use at the Lewis laboratory is described in reference 2. The particular tank shown in reference 2 was used for the tests of engine A. The other three engines were run in three different tanks which vary somewhat in size and description from this tank; these are described in reference 3.



(b) Photograph looking into vacuum tank.

FIGURE 10.—Concluded. Test facility.

A schematic drawing of the general arrangement of engine, electron suppressor screens, hot-wire probes, and condenser baffles is shown in figure 10(a). The end of the engine and the detail of the swinging-arm and traverse actuators for

surveying the beam may be seen. A photograph of the overall arrangement is given in figure 10(b).

Tank pressures in the range 10^{-9} to 10^{-10} atmosphere were used for all engine runs reported herein.

DATA RECORDING PROCEDURE

The hot-wire theory lends itself to two modes of operation, either constant current or constant temperature. The present experimental program was limited to constant-current operation only, because it was the quickest and simplest to perform. The hot-wire heating circuit is shown in figure 11. It consists of a battery and current control resistors. For changes in wire resistance of less than 100 percent, the current in the circuit will be nearly constant. Wire voltage and current were measured with potentiometers as noted in figure 11. The output voltage of the hot wire was fed through an amplifier (which served to isolate the wire and circuit from ground) to an automatic x - y plotter. The x -axis of the plotter is driven by a battery across a variable linear resistor connected directly to the actuators.

EXPERIMENTAL RESULTS AND DISCUSSION

STEADY-STATE MEASUREMENTS

Evaluation of wire physical constants.—The following wire physical constants are required in the theoretical calibration:

- (a) Wire diameter
- (b) Wire length exposed to beam
- (c) Temperature coefficient of resistance

(d) Resistivity

(e) Thermal conductivity

For the present experimental evaluation of the theory, it appeared that a 0.001-centimeter-diameter wire of a platinum-iridium alloy would operate quite well over the range of beam powers expected. A nominal wire length of 0.50 centimeter was chosen for the ion-beam measurements. The wire is available in rolls of about 100 meters, so initial physical-property calibrations are usable over several years. Thus, an elaborate set of initial calibrations can be amortized over a long useful life.

For the physical-property calibrations, it is desirable to measure the diameter and length of test samples carefully. For this report the diameters were measured with a high-magnification laboratory microscope. The lengths were determined using a machinist's microscope and vernier. Experience to date indicates that the particular wire used in the present experiments varies $\pm 0.5 \times 10^{-4}$ centimeter in average diameter along the spool of wire bought commercially. Between two spools of wire, the measured diameter varied $\pm 2.5 \times 10^{-4}$ centimeter between spools which had the same nominal diameter, 10×10^{-4} centimeter.

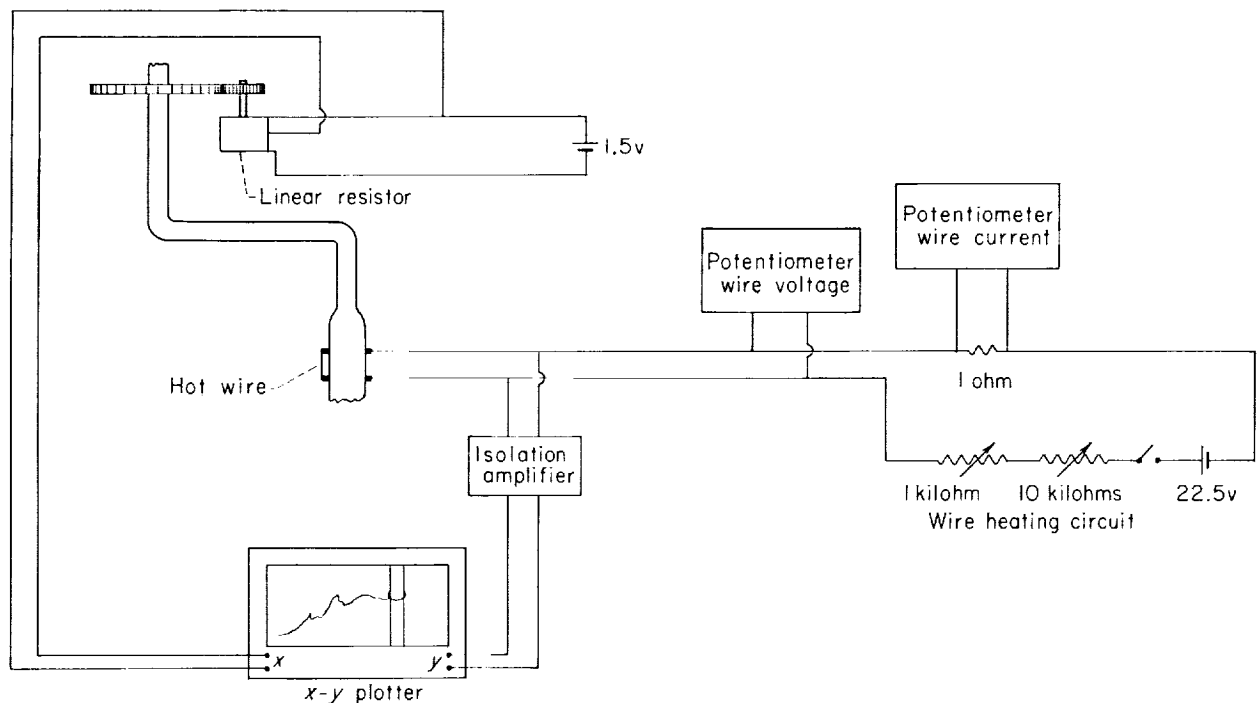


FIGURE 11.—Hot-wire operating and recording circuit.

The remaining physical properties depend on the wire's stress history. It is advisable to anneal all new wire samples after mounting at about 600° to 800° K for 15 minutes to stabilize these physical properties. Annealing is a part of the routine procedure, as well as these initial calibrations.

A method for measuring the temperature coefficient of resistance α in an electrically heated gas furnace is described in reference 11. The data shown in figure 12 were obtained in this furnace.

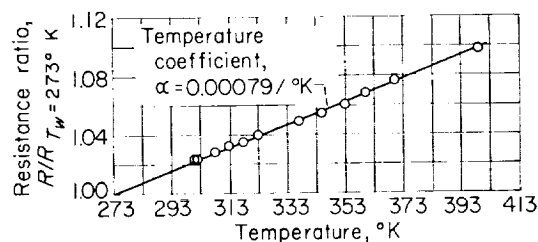


FIGURE 12.—Variation of wire resistance with temperature.

For the present work a simple first-order coefficient α (the slope of the straight line shown in fig. 12) is used to describe the data points. Strictly speaking, the relation between resistance and temperature for all metals is not linear. However, the present theory does not include the nonlinearity, which for platinum-iridium wire is negligible over the temperature range of interest. Further refinements should treat this nonlinearity, which is more pronounced in the temperature range of interest for tungsten wire, for example. Figure 12 is used to evaluate the variation in resistivity with temperature for the wire used in this research.

For the remaining calibrations, a set of wire samples of various lengths is operated over a range of detection currents in a high-vacuum facility. The results of such a test are plotted in figure 13 in the form of resistance as a function of current squared. This form of plot was suggested by equation (11), which is the approximate theoretical calibration for the $jV=0$ case. For convenience, the data are reduced to a support temperature of 273° K by multiplying by the resistance ratio R_0/R_s :

$$R\left(\frac{R_0}{R_s}\right) = R_0 + \left(\frac{R_0}{\alpha_c D l C}\right) I^2 \quad (31)$$

The intercept at $I=0$ in figure 13 is R_0 , the resistance of the wire at 273° K. Thus, for each of the wire samples, a resistivity can be calculated by using the equation

$$\sigma = \frac{\pi D^2}{4l} R_0 \quad (32)$$

The average value obtained in this manner is shown in figure 13, and this is the resistivity used throughout the experimental work reported herein.

The thermal conductivity can be determined from an empirical slope fitted to the data near zero current in figure 13. The slope of equation (31) can be written in terms of the primary variables and rearranged as follows:

$$K = \frac{R_0}{\text{Slope}} \frac{4\sigma\alpha}{3\pi^2} \left(\frac{l}{D^2}\right)^2 \quad (33)$$

The average thermal conductivity determined in this manner is listed in figure 13; this value is used in the subsequent experimental work. The sensitivity of this method can be judged from figure 14, where several theoretical curves (eqs. (7) and (8)) are plotted for thermal-conductivity

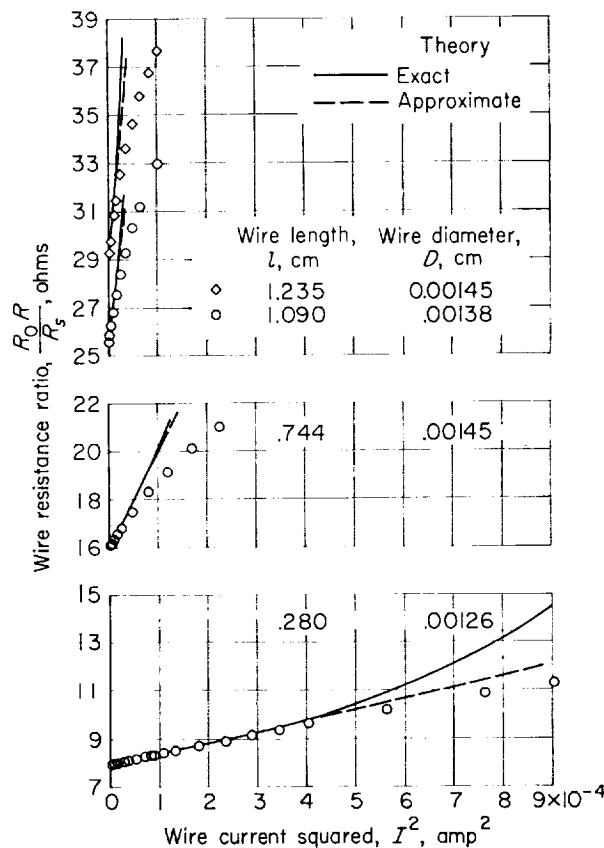


FIGURE 13.—Comparison of heat-transfer predictions with measurements. Wire thermal conductivity, 25.5 w/(m) (°K); wire resistivity at 273° K, 3.57×10^{-7} (ohm) (m).

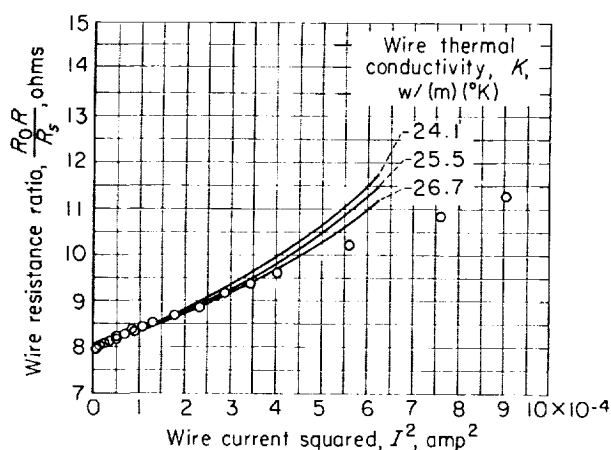


FIGURE 14.—Evaluation of wire thermal conductivity. Wire diameter, 0.00126 centimeter; wire length, 0.280 centimeter.

values of about ± 5 percent of the best fitting value.

Several additional features of figure 13 are worth noting. Two theoretical curves each for the $jV=0$ case are plotted for each wire sample. The solid curves were calculated from equations (7) and (8); the dashed lines were calculated from the approximate theory (eq. (9)). The deviation of the two calculated curves is noticeable at the higher currents and longer lengths (i.e., large $\beta l/2$). The data in figures 13 and 14 also can be used to check qualitatively the systematic error analysis of the section Steady-State Analysis. A variation of the facility pressure from 10^{-8} to 10^{-7} atmosphere did not affect the measured resistances shown in figure 13. This supports the prediction in figure 4(b) which shows that the molecular conduction through the rarefied air is negligible.

Figure 15 shows the approximate radiation error calculated from equations (22) and (23) for the

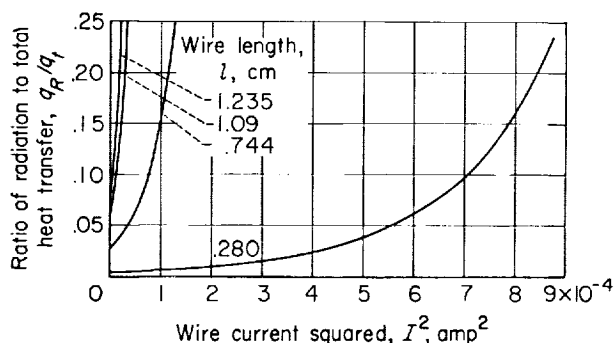


FIGURE 15.—Estimated radiation heat-transfer error for wires used for data of figure 13.

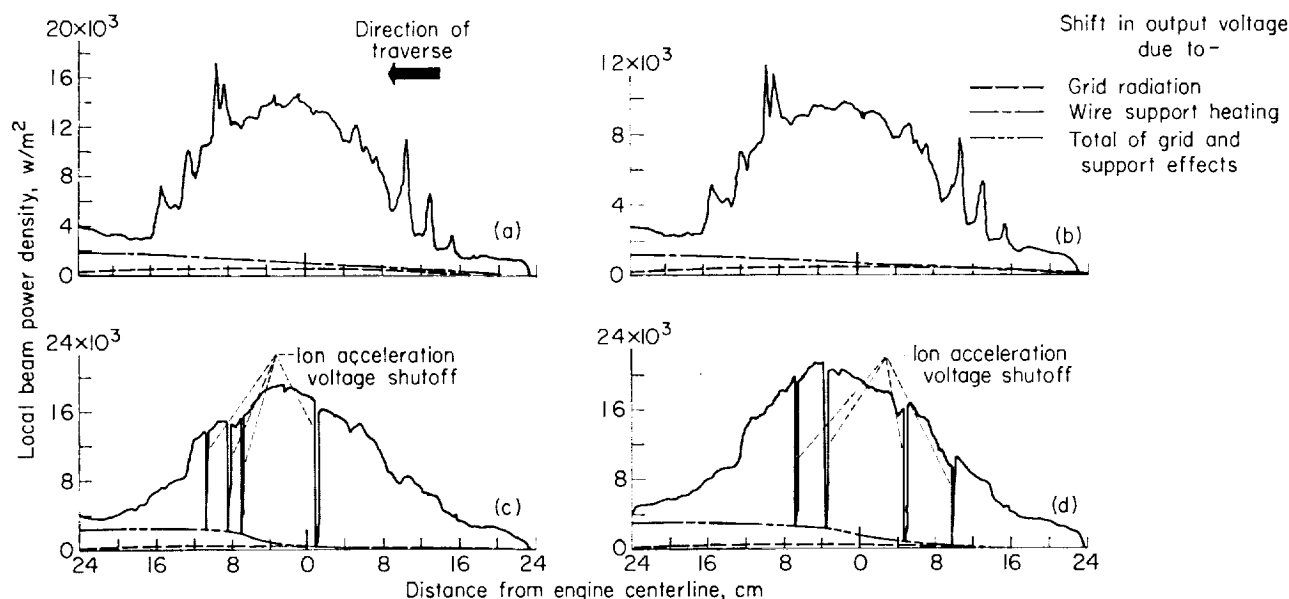
wire samples plotted in figure 13 (assuming $\epsilon=0.10$). The approximate theory predicts that the shortest length will have an appreciable current range with negligible radiation error, while the deviation due to radiation should become progressively pronounced for the longer wires, even for low currents. The data in figure 13 qualitatively substantiate these predictions. The measured resistance (temperature) falls systematically below theory because the radiation heat loss has been neglected. These data also show that it is possible to have a practical detection current range with negligible radiation error, if care is taken in the probe design.

The physical properties evaluated for the present platinum-iridium wire listed in table I differ somewhat from previously published values. Reference 12 gives values for the physical constants of 80-percent-platinum—20-percent-iridium wires which were used in the calculations of the theory section (figs. 3 to 7). The present evaluation of constants suggests that the wire material used in this investigation differs from the 80–20 proportions.

The routine calibration procedure is effectively an indirect experimental measure of wire diameter. It is impractical to measure the diameter of each wire with a laboratory microscope, particularly when the hot-wire rakes are semipermanently mounted in the vacuum tank. However, if the wire length is measured with a clamp-on microscope while the rake is in place, the effective wire diameter can be calculated from both the intercept and the slope of calibration data such as figure 13, because σ , α , and K are known from the initial calibrations. This procedure is demonstrated in appendix C.

Operation in ion beams.—Present experience with hot wires in ion beams has been in direct connection with the understanding and improvement of ion engine performance rather than probe design. While a wide range of high-energy ion beams has been probed, the data presented do not represent a truly systematic set of probe operating conditions. Direct comparison of hot-wire results with other measurements can only be made for the overall effects, because no other “point” probes are developed at this time. Thus, it is difficult to assess the accuracy of the individual measurements.

A typical set of surveys across the ion beam produced by engine A is shown in figure 16. All the profiles were made by the same wire traveling



(a) Wire diameter, 0.00118 centimeter; engine conditions: 20-kilovolt ionizer; 20-milliampere beam current.
 (b) Wire diameter, 0.00114 centimeter; engine conditions: 20-kilovolt ionizer; 19-milliampere beam current.
 (c) Wire diameter, 0.00111 centimeter; engine conditions: 16-kilovolt ionizer; 41-milliampere beam current.
 (d) Wire diameter, 0.00109 centimeter; engine conditions: 20-kilovolt ionizer; 41-milliampere beam current.

FIGURE 16.—Hot-wire surveys across ion beams.

across the beam at the same location at different engine conditions. This wire was on the traversing screw actuator 46 centimeters downstream of the engine exit and on the centerline of the engine. The hot-wire calorimeter was experiencing sputtering, so that a slight change in wire diameter is noted for each profile. The effect of sputtering and the method of computing wire diameter are given in detail in appendix C.

For each profile the power due to thermal radiation from the hot tungsten ionizers is noted as the dashed curve. The thermal radiation power must be subtracted from the total reading to find ion-beam power density. Also noted is the shift in the effective-power-density zero point caused by the inadequate cooling of the wire supports. This zero shift must also be taken into account in computing the local power density. These operating problems are more fully considered in appendix C.

Figure 16 demonstrates the types of ion beams encountered under different operating conditions. The repeatability of local peaks in measured power density is found to be very consistent, at a fixed engine condition, as may be seen in figures 16(a) and (b), which were taken about an hour apart.

Figures 16(c) and (d) demonstrate the effect of shutting off the accelerator voltage on the engine. The data show that the hot-wire output is due to the ions which were accelerated through the high-potential electrodes. The quick removal of accelerator voltage is an accurate method of establishing the base value of voltage for the wire at any time in a survey. Figure 16(d) suggests that the hot wire might be employed as a sensitive instrument to maintain constant beam power.

By taking several surveys at one time within the beam, it is possible to construct a complete map of the ion beam. Figure 17 shows a set of surveys taken with the swinging-arm probe. All five surveys were taken at the same time and at the same distance downstream of the engine. The probes are located 2.5 centimeters apart with probe number 3 located approximately on the centerline of the engine. The dashed curve in each figure is the estimated zero shift caused by radiation from the ionizer and heating of the supports. There is a slight shift in scale factor from plot to plot because of the variation in electronic amplifying equipment. The abscissa indicates distance in centimeters normal to the engine

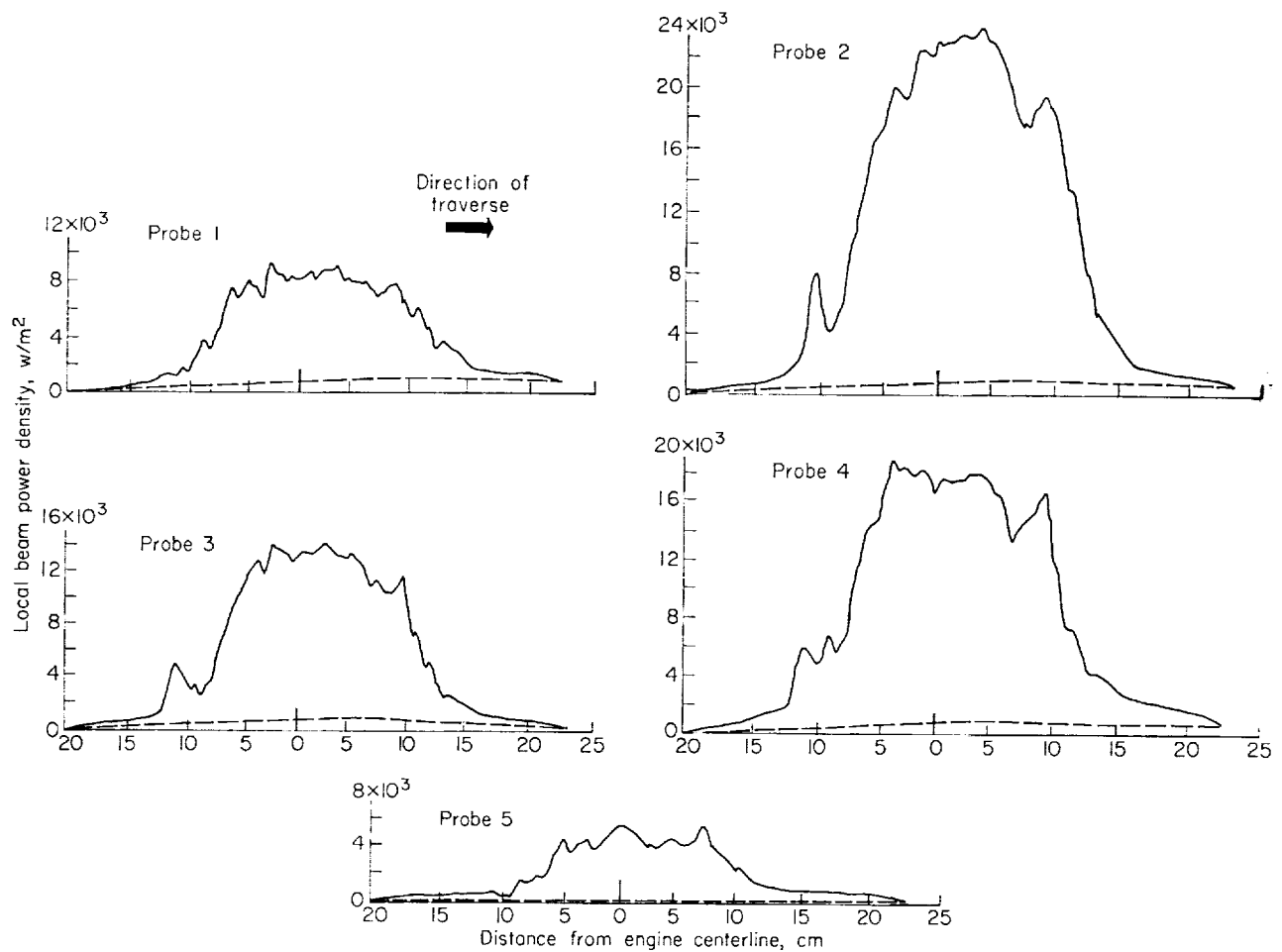


FIGURE 17.—Set of hot-wire surveys taken at different vertical locations in ion beam. Probes 2.54 centimeters apart, 20.97 centimeters downstream of second electrode; probe 3 approximately on engine horizontal centerline.

centerline. The probes were moved with a 35-centimeter arm, so that the outer edges of the profile are closer to the engine exit than the center. Figure 18 is a contour map constructed from the data of figure 17.

The contour map of figure 18 shows the number of peaks in power density which can be encountered in an engine such as engine A. While the exact shape of the local maximums may not be as pictured in figure 18, this figure does indicate the regions of needed investigation within the engine geometry. The dashed portion of the map represents the area of least certainty. In most instances, the lines drawn represent at least two points and a reasonably established boundary condition.

Details of ion-beam spreading are also being investigated with the hot-wire calorimeters. Figure

19 shows two contour maps taken in the same beam at two downstream locations. Figure 19(a) is for an ion beam with an estimated power of 640 watts, which was calculated from engine current and potential meters; figure 19(b) has an estimated power from meters of 218 watts. At each of these beam powers, the detail available at the station 46 centimeters downstream is limited by the wider probe spacing and low power density. However, it is possible to identify some of the corresponding local peaks in power density.

To test the measurement of beam power density indicated by the hot wires, the total integrated power of the beam can be computed from the contour map. The power obtained from these integrations is listed above each contour map in figure 19. Considering the fairing required in the contour maps and the arbitrary cutoff at 1030

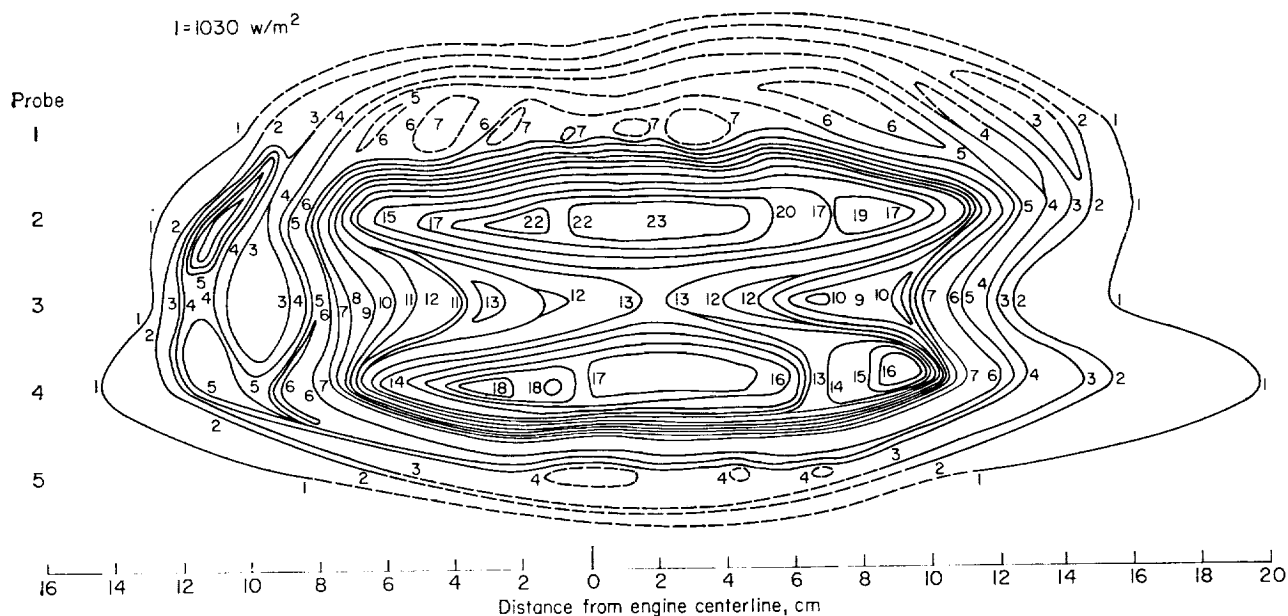


FIGURE 18.—Contour map of lines of constant power density in ion beam. Surveys given in figure 17.

watts per square meter, the agreement between the integrated total power of the front and back maps is good at both power levels. A comparison of metered power and the hot-wire measured power shows good agreement at the local power level, but in figure 19(a), the deviation is about 30 percent. However, limited measurements obtained to date show no systematic variation of hot-wire results with current density, and in general, the agreement between engine metered power and hot-wire measurements is about ± 10 percent. It is not reasonable at present to regard the metered power readings as absolute values for comparison. Furthermore, the agreement between total power found from hot-wire maps and that measured by 2-inch-square copper-sheet calorimeters is good.

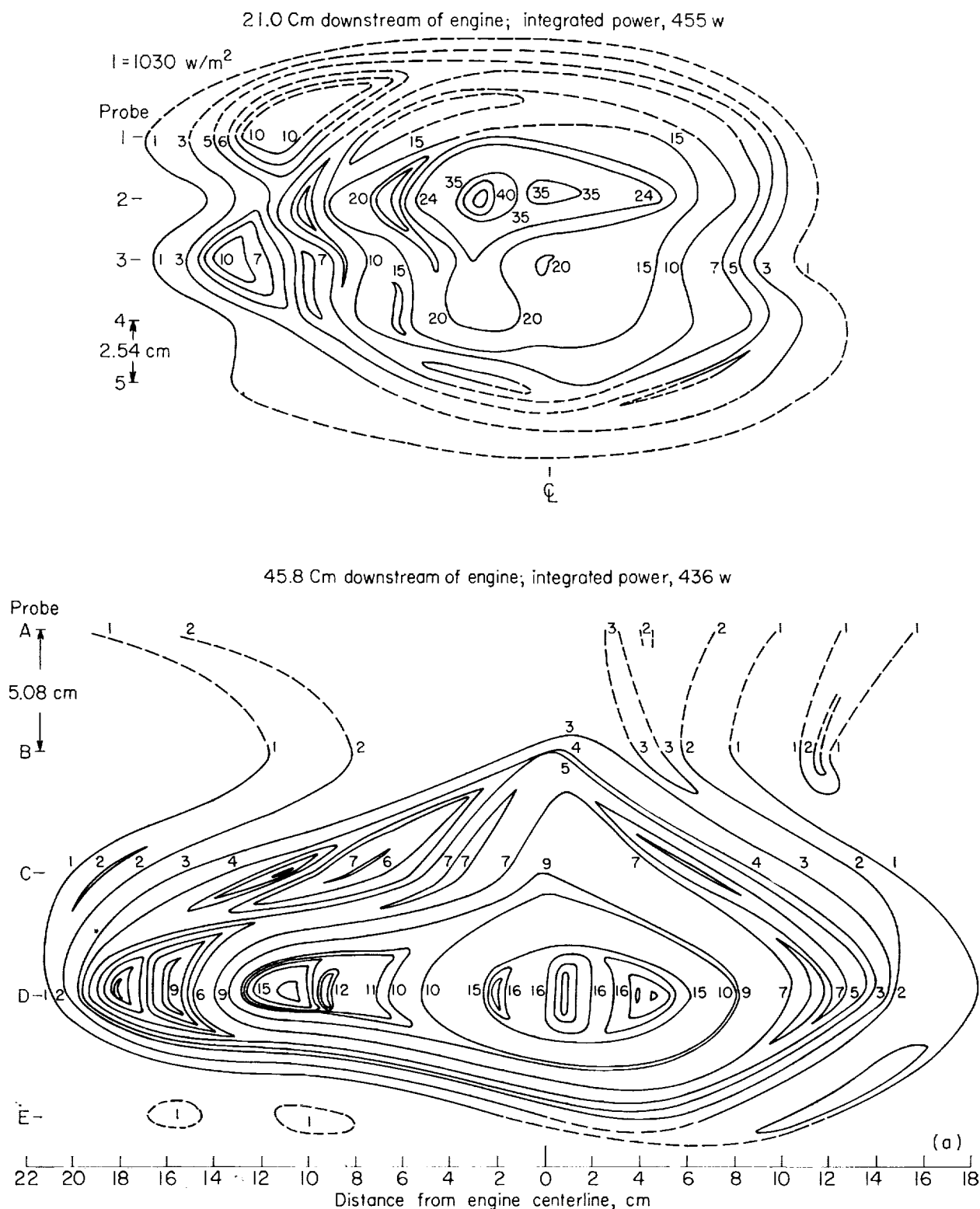
The present ion-beam data were selected to demonstrate, as much as possible, the consistency of the present approach to ion-beam measurements. It is again noted that the data are certainly inadequate to establish all factors in the probe operation. However, the present approach has advanced farther than any other diagnostic technique now being used in the present test facilities. Experience in engines other than engine A is accumulating rapidly. Some surveys from other engines listed in the apparatus table are shown in figure 20. All the engines shown in

figure 20 operate at much lower voltage levels than engine A, and they tend to have much smoother power-density distributions. The hot wires have proved quite useful in demonstrating beam stabilizing and local focusing for these lower voltage engines. An example of the beam stabilizing effect of an immersed, hot-cylinder electron emitter described in reference 10 is shown in figure 21. Present ion engine development work is concerned with overall power output, rather than with detailed studies, so that the probes should be of even more value in the future.

Hot-wire-calorimeter rakes are now in routine operation in the three large vacuum facilities devoted to electric rocket research at this laboratory. The data presented herein are samples chosen to demonstrate certain aspects of the probe application. Later reports concerned with the design and testing of specific engines will present more detailed data on comparative instrumentation and the interpretation of beam surveys in terms of engine design.

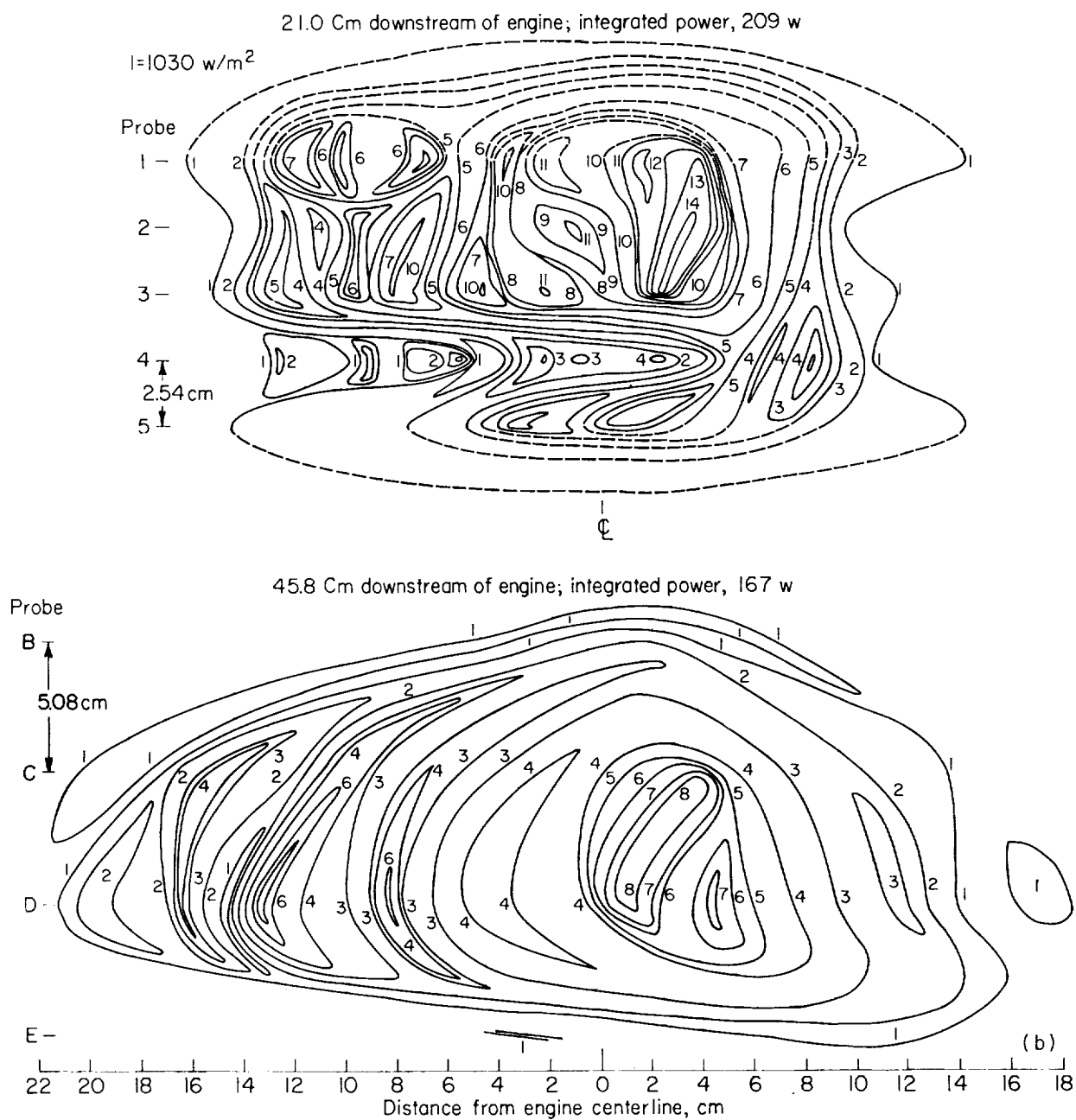
TRANSIENT MEASUREMENTS

Once the steady-state operation of the probe is understood, it is logical to consider the hot wire as a transient measuring instrument. Since the present method of heat loss is different from that of the familiar hot-wire anemometer, response



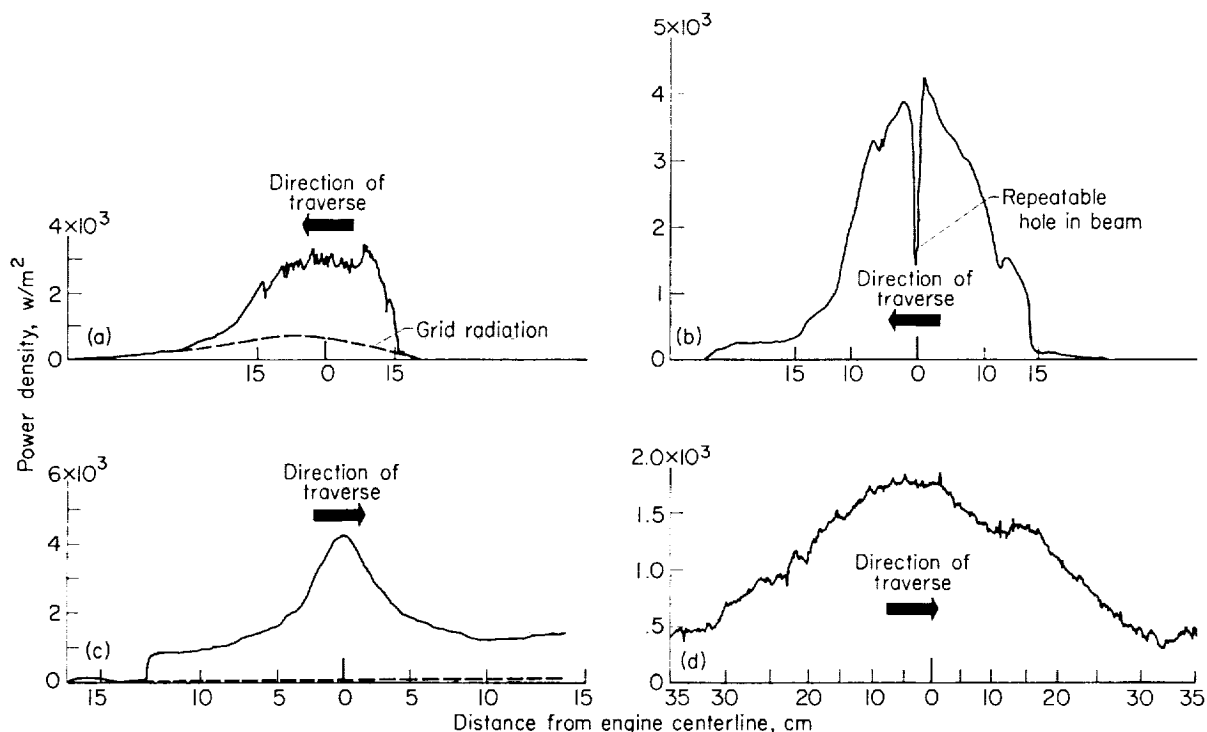
(a) Acceleration voltage, 16 kilovolts; estimated power from meters, 640 watts.

FIGURE 19.—Comparison of ion-beam contour maps at two locations downstream of engine.



(b) Acceleration voltage, 16 kilovolts; estimated power from meters, 218 watts; engine screen.

FIGURE 19.—Concluded. Comparison of ion-beam contour maps at two locations downstream of engine.



(a) Engine B. Acceleration voltage, 200 volts; estimated power, 7 watts.
 (b) Engine C. Operating conditions not recorded.
 (c) Engine D. Acceleration voltage, 10,000 volts; estimated power, 135 watts.
 (d) Engine E. Acceleration voltage, 500 volts; estimated power, 10 watts.

FIGURE 20.—Hot-wire surveys taken in different engines and facilities.

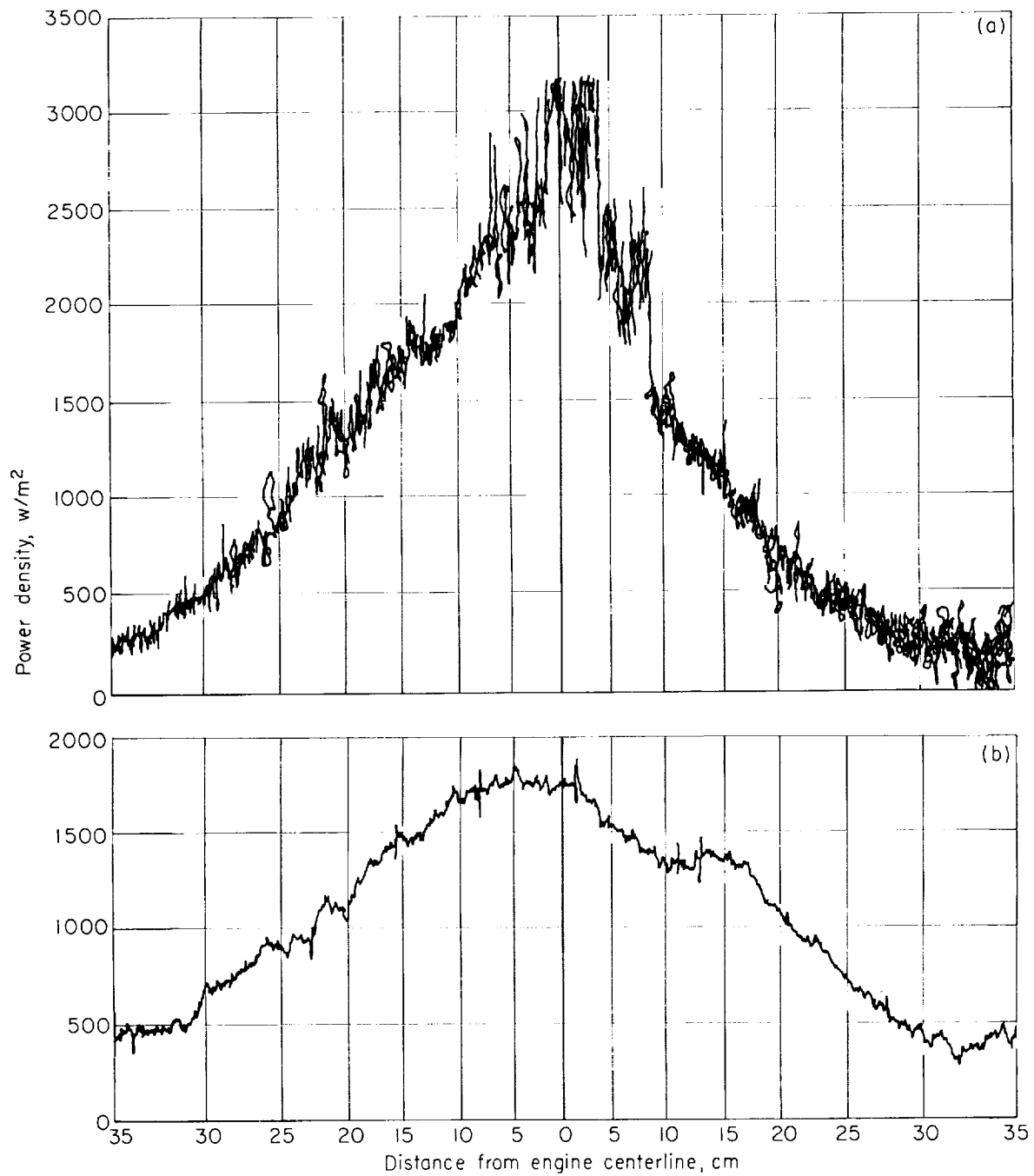
of the wire in this new application to changes in environment does not parallel the anemometer application. No doubt the electronic circuits developed for fluid-flow anemometers can be employed in the present application to improve the transient response time of the wires.

A few check measurements of wire response time for the special case where the initial operating current is zero have been made. The measurements may be compared with that special case of the transient analysis. Figure 22 compares the measured time response curves with theoretical predictions at several different currents. The initial jump in voltage for a step current to that voltage corresponding to the "cold" wire resistance is not shown, since it would serve only to indicate the time response of the electronic circuit (this initial step was measured at less than 2 micro-seconds). The agreement between measurements and predictions is fairly good in the low-current range, where radiation can be neglected. Figure 14, wherein the value of thermal conductivity is

evaluated, is the steady-state calibration of the wire used to obtain the data of figure 22. Figure 14 shows that the effects of radiation become important above a current of 15 milliamperes. Thus, the disagreement between the predicted and observed curves in figure 22(c) may be attributed to radiation.

The time constant is plotted against the current step in figure 23 along with the theoretical value. The deviation from the theoretical curve at low current steps is believed to be due to readability of the traces. The deviation of the theoretical and measured values above 15 milliamperes is due to radiation and corresponds very closely to the deviation of theory and experiment in figure 14, which is the steady-state data for the same wire.

The temperature-time analysis can predict the transient curve well when the wire constants are known as in this example. The time-constant analysis requires in addition to the previously discussed physical properties a knowledge of the specific heat and the density of the wire material.



(a) Electron emitter off.

(b) Electron emitter on.

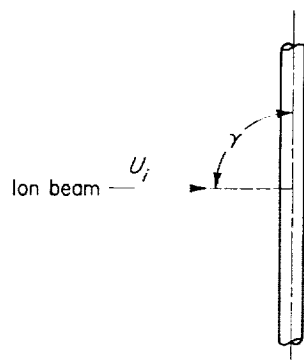
FIGURE 21.—Beam stabilization by electron addition. Engine E.

Handbook values of these properties, as listed in table I, were used in the theoretical calculations of this section.

POSSIBLE FUTURE APPLICATIONS

YAWED WIRES

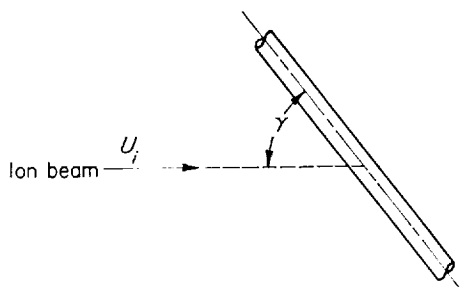
In both the analysis and the experimental work reported here, the hot-wire-calorimeter axis has been implicitly assumed to be normal (90°) to the ion velocity vector as shown in sketch (a):



(a)

Sketch (a)

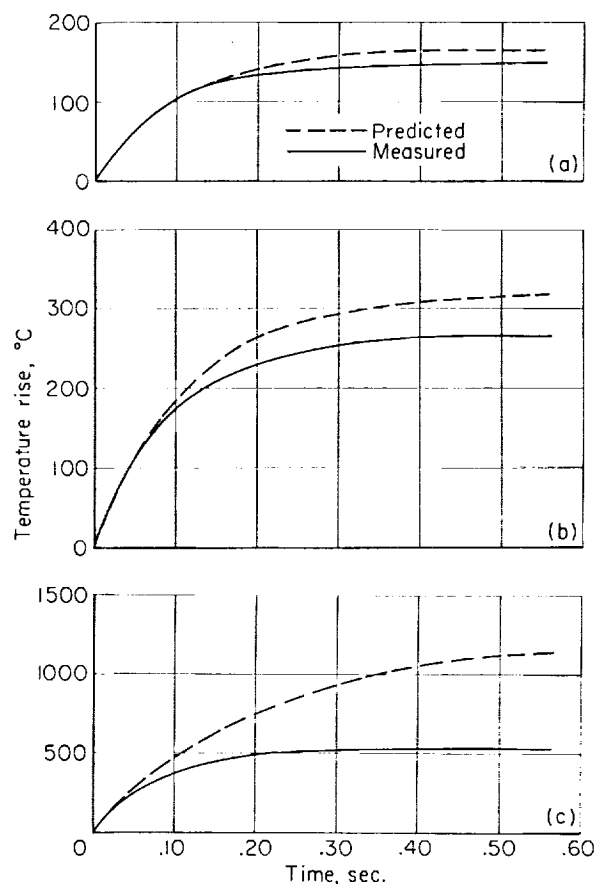
However, the analysis is easily extended to the more general case shown in sketch (b), where the wire is yawed or inclined at an angle γ to the ion velocity:



(b)

Sketch (b)

Appendix B outlines this modification to the original analysis. The net result is to change the local power density in all the equations from jV to $jV \sin \gamma$. This means that the hot-wire calorimeter is directionally sensitive to ion velocity and that a systematic variation of the probe angle can be used to find the velocity vector angle of a uni-directional ion beam. For a constant-current calorimeter, a plot of wire voltage against angle of



(a) Change in wire current, 0.015 ampere.

(b) Change in wire current, 0.020 ampere.

(c) Change in wire current, 0.030 ampere.

FIGURE 22.—Comparison of predicted and observed time response curves.

probe rotation should follow a sine law. Deviation of experimental data from this behavior for angles between 30° and 90° might be traced either to wire support interference or to appreciable random ion velocities transverse to the mean direction. This application is somewhat reminiscent of the use of hot-wire anemometers in aeronautical research (e.g., ref. 12). Although no experimental research has been attempted to date on yawed hot-wire calorimeters, the application should be straightforward.

INDEPENDENT MEASURE OF CURRENT DENSITY

In some future applications, it may be of interest to measure the current density j separately from the power product jV . Use of a Faraday cup is one method which has been tried for this purpose in physics laboratory experiments with

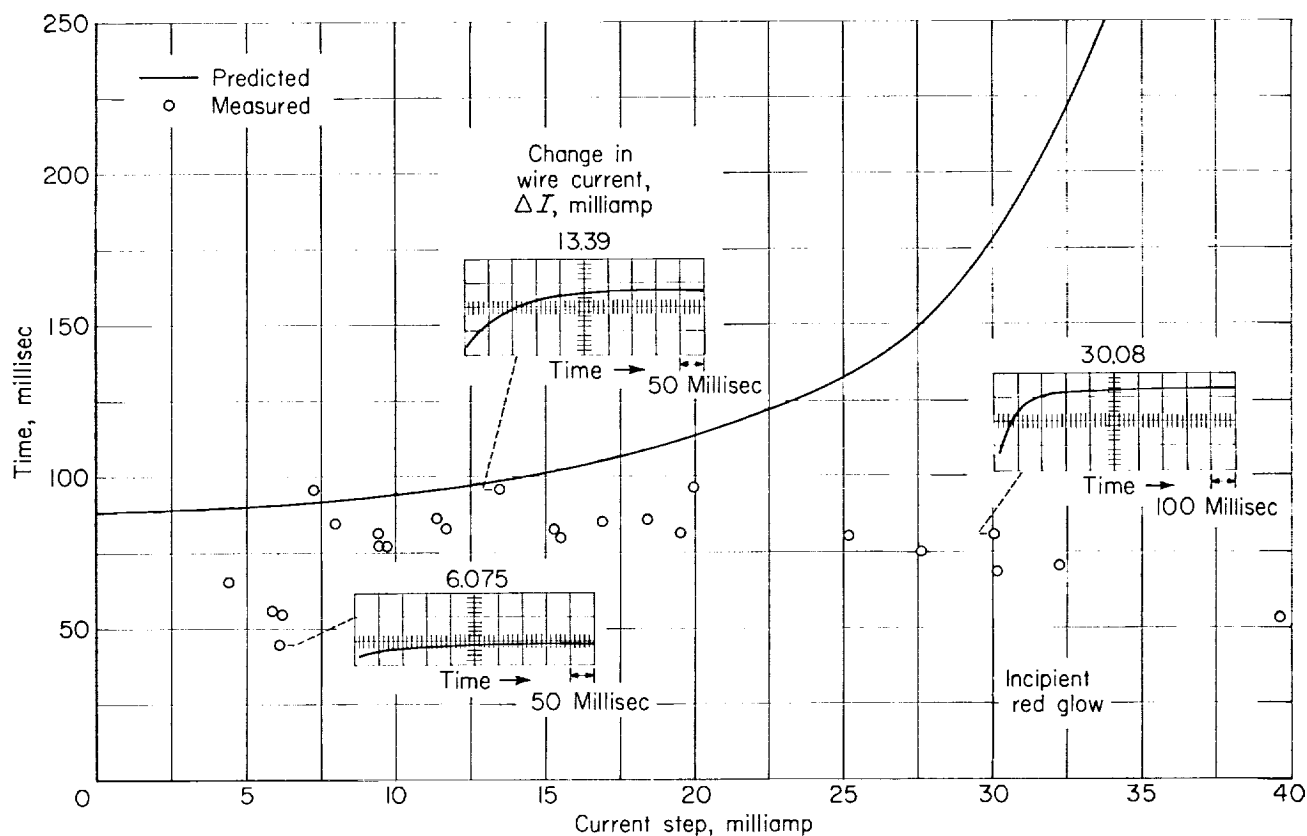


FIGURE 23.—Comparison of predicted and measured time constants for 0.001-centimeter-diameter platinum-iridium wire.

ion beams. However, the application of a small sampling Faraday cup to ion rocket research is complicated, and to the best of our knowledge no detailed reports on this subject have been published, although work is continuing on this measurement technique. Depending somewhat on the success of this Faraday cup work, it may be interesting to develop a method using the transient response of the hot-wire calorimeter for ion velocity measurements. One possible scheme for doing this is outlined in the following paragraph.

In an ion beam which is operating substantially neutralized by free electrons, a pulse of the accelerating voltage (at constant ionizer voltage) should propagate as a pulse in ion power density down the beam at the ion velocity. Ion velocity will be unchanged if ionizer voltage and overall V is unchanged. This pulse in local power will move much too rapidly for a hot-wire calorimeter to follow. However, by placing two probes having matched time constants in the beam, one a distance Δz closer to the accelerator than the other, it might be possible to use the hot wires as triggers

for a timing circuit. The measurement of the time interval Δt , together with wire spacing Δz , would make it possible to calculate an average ion velocity U_t . The ion velocity is simply related to the effective accelerating voltage V , so the measurement of the steady-state power density jV would make it possible to calculate the current density j .

CONCLUDING REMARKS

The need for new instruments suitable for experimental research in low-density high-energy ion beams that may find application to future space propulsion motivated this research. The following conclusions may be drawn:

1. A steady-state analysis of the probe sensitivity relates the local power density of an ion beam to the voltage output of a fine wire with an external detection current. The change in resistance of the wire is due to the conversion of the ion kinetic energy to heat at the wire surface. The beam power together with the joulean heat rate is balanced by conduction along the wire to

cooled supports at each end. The probe is called a hot-wire calorimeter.

2. Experiment verified the theoretical predictions of characteristics of the hot-wire calorimeter when it is operated out of the ion beam in the vacuum of the test facility. The measurement of the wire resistance for a range of detection currents, when the wire is out of the beam, serves as a convenient calibration of the hot-wire calorimeter to the ion-beam power, assuming that the effective accommodation coefficient is known. The data also demonstrate that both the thermal radiation error and error due to molecular conduction to surrounding air can be made negligible as the theory predicted.

3. Experimental data have been obtained using the hot-wire calorimeters in cesium and mercury ion beams with total beam currents up to 100 milliamperes and over a range of accelerating voltages from 1 to 20 kilovolts. No other instrument of comparable size is available at this time to make detailed ion-beam surveys. Therefore, attempts to determine the hot-wire-calorimeter accuracy by comparative instrumentation must be limited at this time to spatial integrations of hot-wire beam surveys for comparison with large calorimeters and ion rocket potential and current meters. Preliminary experiments indicate that: (a) the hot-wire calorimeter can consistently repeat ion-beam power-density profiles with negligible error, and (b) spatial integrations of hot-wire-calorimeter beam surveys compare reasonably well with both large-calorimeter data and meter readings.

4. The text reviews the primary practical problems which have been incurred in the first 6 months of operating hot-wire calorimeters at this laboratory. Among the problems discussed together with working solutions were: (a) probe support heating, (b) sputtering and its relation to the effective accommodation coefficient and calorimeter calibrations, and (c) secondary electron emission and the related problems of stray current pickup, probe biasing potential, and sampling cross-sectional area.

5. An analysis is presented for the transient response of the hot-wire calorimeter to step changes in power input. Experimental data agreed with theoretical calculations. The response characteristics are essentially those of a first-order system in both theory and experiment, so that transient characteristics are given by a single time constant. With compensating amplifiers comparable to hot-wire anemometers familiar in aeronautics, a usable frequency response of at least zero to 10,000 cycles per second should be possible.

6. The extension of hot-wire calorimeters to two additional measurement techniques is discussed. By varying the angle of incidence of a hot-wire calorimeter to the ion beam, the direction of the ion velocity vector may be found. Two matched hot wires could be used in pulsed, neutralized ion beams in a time-of-flight technique for the measurement of average ion velocity.

LEWIS RESEARCH CENTER

NATIONAL AERONAUTICS AND SPACE ADMINISTRATION
CLEVELAND, OHIO, December 13, 1960

APPENDIX A

SYMBOLS

a_c	accommodation coefficients in eq. (B17)	N_A	Avogadro number, 6.0235×10^{26} mol-ecules/kg-mole
B	constant defined by eq. (9), v	n	a digit
C	constant defined by eq. (9), amp ² /m ²	p	ambient pressure surrounding wire, atm
c	wire specific heat, j/(kg)(°K)	Q	heat-flow rate from wire, w
c_p	specific heat of monatomic gas, j/(kg)(°K)	q	axial heat-flow rate per unit length of wire at station x , w/m
D	wire diameter, m	R	resistance of wire having average temperature T_w , ohms
E	voltage difference across wire, v	R_r	reflected primary ion ratio
e	charge of ion, \mathcal{F}/N_A , coulombs	R_s	resistance of wire having average temperature T_s , ohms
\mathcal{F}	Faraday's constant, 9.6469×10^7 coulombs/kg-mole	\mathcal{R}	universal gas constant, 8314 j/(kg-mole)(°K)
$f^\circ(s)$	dimensionless function of s , $(s^2+2)\pi e^{-(s^2/2)} I_0\left(\frac{s^2}{2}\right) + \left(s^2 + \frac{5}{2}\right)\pi s^2 e^{-(s^2/2)} \left[I_0\left(\frac{s^2}{2}\right) + I_1\left(\frac{s^2}{2}\right) \right]$	r	resistance of wire per unit length, ohms/m
$g^\circ(s)$	dimensionless function of s , $2\pi e^{-(s^2/2)} I_0\left(\frac{s^2}{2}\right) + 2\pi s^2 e^{-(s^2/2)} \left[I_0\left(\frac{s^2}{2}\right) + I_1\left(\frac{s^2}{2}\right) \right]$	S	sputtering ratio, atoms sputtered/ion incident
h	heat-transfer coefficient, w/(sq m) (°K)	s	molecular speed ratio, U/v_m
I	wire current, amp	T_a	temperature of gas surrounding wire, °K
I_0, I_1	modified Bessel function of first kind, zero and first order, respectively, dimensionless	T_i	ionizer temperature, °K
j	ion-beam current density, amp/m ²	T_s	temperature of wire support, °K
K	wire thermal conductivity, w/(m) (°K)	T_w	length-average wire temperature, °K
K^+	secondary positive ion ratio	$T_{w,\infty}$	term having units of temperature, $(\beta_i/\beta)^2$, °K
K^-	secondary negative ion ratio	$T_{w,\infty}$	term having units of temperature, $(\eta_i/\eta)^2$, °K
L	distance of probe from inlet plane (fig. 24), m	t	time, sec
l	wire length, m	t_w	local wire temperature at station x , °K
M_i	molecular weight of incident ion, kg/kg-mole	U	velocity of ion, m/sec
M_a	molecular weight of ambient gas, kg/kg-mole	u	variable of integration in eqs. (B45)
M_w	molecular weight of wire material, kg/kg-mole	V	net accelerating voltage of ion beam, v
m	mass, kg	v	variable of integration in eq. (B45)
		v_m	most probable molecular speed, $\sqrt{2\mathcal{R}T/M}$, m/sec
		W	energy, w-sec or j
		w	energy per particle, j/atom
		x	distance along wire measured from center of wire, m
		Y	distance (fig. 24), m
		Y_c	effective sampling diameter of biased probe, m

y	distance (fig. 24), m	μ	mass of ion, M_i/N_A , kg
Z	distance (fig. 24), m	ρ	wire density, kg/cu m
z	distance (fig. 24), m	σ	wire resistivity at 273° K, (ohm) (m)
α	temperature coefficient of resistance, 1/°K	σ_{SB}	Stefan-Boltzmann radiation constant, w/(sq m) (°K) ⁴
β	constant in eq. (5), $\sqrt{\left(\frac{4}{\pi D^2}\right)^2 \frac{\sigma\alpha}{K} I^2}$, 1/m	τ	constant of integration in eq. (B47), $\frac{\rho c}{\sigma\alpha} \left(\frac{\pi D^2}{4}\right)^2 \frac{1}{I^2}$, sec
β_0	constant in eq. (28), $\sqrt{\left(\frac{4}{\pi D^2}\right)^2 \frac{\sigma\alpha}{K} I_0^2}$, 1/m	τ_E	effective time constant in eq. (29), sec
β_1	constant in eq. (5), $\sqrt{\frac{a_c D j V}{K \left(\frac{4}{\pi D^2}\right)} + \left(\frac{4}{\pi D^2}\right)^2 \frac{\sigma\alpha}{K} \left(\frac{1}{\alpha} - 273\right) I^2}$, (°K) ^{1/2} /m	Φ	ratio of heat loss by conduction to supports to heat loss to ambient gas
μ_2	constant in eq. (20), $\sqrt{\frac{\sigma_{SB}\epsilon}{K} \frac{4}{D}}$, m/(°K) ²	Subscripts:	
γ	angle of incidence	B	beam heating
γ_{el}	secondary electron emission ratio	e	recovery
δ	error ratio	el	electron
ϵ	gray-body or total emissivity	FM	free molecule
η	constant in eq. (15), $\sqrt{\frac{4h}{\pi D} - \left(\frac{4}{\pi D^2}\right)^2 \frac{\sigma\alpha}{K} I^2}$, 1/m	G	ground
η_1	constant in eq. (15), $\sqrt{\frac{4hT_a}{KD} + \frac{a_c D j V}{K \left(\frac{4}{\pi D^2}\right)} + \left(\frac{4}{\pi D^2}\right)^2 \frac{\sigma\alpha}{K} \left(\frac{1}{\alpha} - 273\right) I^2}$, (°K) ^{1/2} /m	i	ion
θ	variable of integration in eq. (B24)	J	joulean or ohmic heating
λ_n	wave number of eigenvalue solution for eq. (27), $\frac{2(n\pi + (\pi/2))}{l}$, 1/m	K	conduction along wire
		n	a digit
		R	radiation
		r	reflected
		S	storage
		SB	Stefan-Boltzmann
		s	support
		sec	secondary
		sp	sputtered
		t	total
		w	wire
		θ	angular
		0	initial value
		Superscripts:	
		0	neutral
		$+$	positive
		$-$	negative

APPENDIX B

ANALYSIS

STEADY-STATE EQUATIONS

The text attempts to emphasize that the ultimate accuracy attainable with hot-wire calorimeters depends on two factors: (1) the correct calculation of the wire cross-sectional area for the interception of the high-energy ions, and (2) the ability to predict accurately the efficiency of conversion of ion kinetic energy to heat at the wire surface. The remainder of the hot-wire-calorimeter properties are not only easily calculated but also conveniently calibrated before each experiment. The main portion of this appendix is devoted to the theoretical aspects of these two factors; the remainder deals with analytical detail.

Heat transfer to wire.—The model chosen for the original calculations was no doubt a result, in part, of the authors' past technical background. This physical model, a classical one in aerodynamics, is instructive and will be given here. Consider the flow of monatomic, neutral particles over the surface of a normal cylinder whose diameter is a small fraction of a mean free path. The flowing gas has the Maxwellian velocity distribution of a gas at temperature T_i superimposed on its directed motion. The energy balance on the fine wire is given in detail in reference 13, and the resulting heat-transfer coefficient h_i can be written as follows:

$$h_i = \frac{p v_m a_c g^o(s)}{2(0.987 \times 10^{-5}) \pi^{3/2} T_i} \quad (\text{B1})$$

The net heat transfer from the flowing gas to the cylinder is defined as

$$Q_B = h_i \pi D l (T_e - t_w) \quad (\text{B2})$$

Note that the heat-transfer coefficient h_i is a function of: (1) the atomic arrival rate $(p/T_i)v_m$ for the no-flow case, (2) the function $g^o(s)$, which depends on the cylindrical geometry and the nondimensional speed of the flow s , and (3) the accommodation coefficient a_c for effectiveness of the energy transfer in the atom-surface collision. The symbol T_e in equation (B2) is the recovery temperature of the gas on the cylinder. The

classical theory outlined in reference 13 relates T_e to the total temperature T_t as follows:

$$T_e = \left[\frac{T_i f^o(s)}{T_t g^o(s)} \right] T_t \quad (\text{B3})$$

where

$$T_t = T_i + \frac{U^2}{2c_p} \quad (\text{B4})$$

For the ion-beam application where the ions are formed by surface ionization, the gas temperature T_i is the surface emitter temperature. The statistical theory of surface ionization assumes that the ions formed have a Maxwellian temperature distribution (e.g., ref. 5), just as in the model being used here. But the ion kinetic energy due to electrostatic acceleration will be very large compared with this random thermal energy imparted by the emitter temperature. For example, for cesium ions,

$$\text{Directed velocity: } U = 1204 \sqrt{V} \text{ (m/sec)}$$

$$\text{Thermal velocity: } v_m = 11.18 \sqrt{T_i} \text{ (m/sec)}$$

where T_i is in °K and V is in volts. For an emitter operating at 1400° K, the kinetic-energy term in equation (B4) becomes dominate for all $V > 100$ volts. So, for a high-energy ion beam accelerated by a voltage V ,

$$T_t = \frac{U^2}{2c_p} = \frac{\mathcal{F}}{c_p M_i} V \quad (\text{B4b})$$

In equation (B3) the functions $f^o(s)$ and $g^o(s)$ depend on the molecular speed ratio s :

$$s \equiv \frac{U}{v_m} \quad (\text{B5})$$

As discussed previously, U is large, and it is conservative to limit the discussion to $s > 4$. The bracketed group in equation (B3) closely approaches an asymptotic value of 5/4 for $s > 4$ (ref. 13). Combining equations (B3) and (B4b) gives

$$T_e = \frac{5}{4} T_t = \frac{5}{4} \frac{\mathcal{F}}{c_p M_i} V \quad (\text{B6})$$

Equation (B1) can be rewritten in terms of the ion current density j :

$$\rho U = \frac{M_i}{\mathcal{F}} j \quad (\text{B7})$$

The perfect-gas law and the specific-heat relation, for monatomic gases, is used to reduce the equations

$$\rho = \frac{M_i p}{(0.987 \times 10^{-5}) \mathcal{R} T_i} \quad (\text{B8})$$

and

$$c_p = \frac{5}{2} \frac{\mathcal{R}}{M_i} \quad (\text{B9})$$

Combining equations (B1), (B5), (B7), and (B8) gives the desired relation when the asymptotic value of $g^\circ(s)/s = 4\sqrt{\pi}$ given in reference 13 is used:

$$h_i = j \left(\frac{a_c 2 \mathcal{R}}{\pi \mathcal{F}} \right) \quad (\text{B10})$$

The hot-wire calorimeter will always operate with a t_w lower than the surface ionizer temperature, so the same argument which led to equation (B4b) can be used to drop t_w compared with T_e in equation (B2):

$$Q_B = h_i \pi D l T_e \quad (\text{B11})$$

Substituting equations (B6), (B9), and (B10) into equation (B11) gives the equation for the beam power input to the wire which is used in the text:

$$q_B = \frac{Q_B}{l} = a_c D j V \quad (\text{B12})$$

Two aspects of the model which led to equation (B12) need to be examined in more detail. First, the beam is composed of ions and the hot-wire calorimeter can, in general, act as a focusing electrode and exert a force on the ions, which would affect the sampling cross-sectional area and the kinetic energy of the incident ions. Secondly, the accommodation coefficient in equation (B12) for the high-energy ion beam must not be confused with the classical numerical value, because the ion-surface interaction is entirely different.

Effective cross-sectional area of wire.—A first approximation to the focusing electrode problem just noted is outlined here. The problem is depicted in figure 24. An infinitely long wire of diameter D is operated at a variable potential V_w measured relative to ground. At some distance L (where $L \gg D$) positive ions which

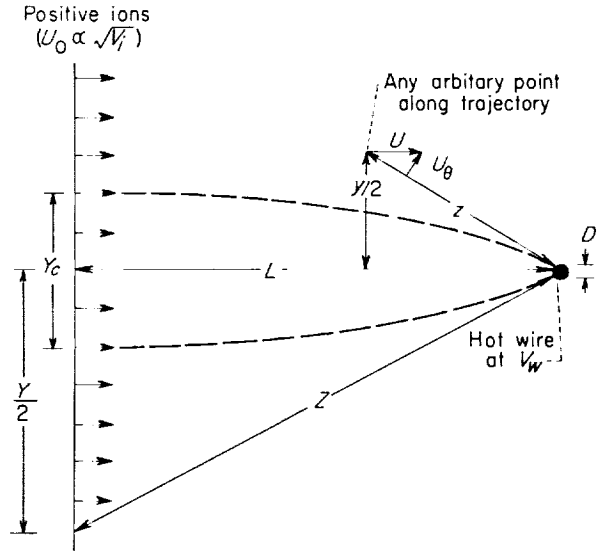


FIGURE 24.—Ion interception by cylindrical electrode.

have been accelerated through a positive potential V_i enter with uniform velocity. The problem is: given values of V_w and V_i , what fractional width of the beam Y_c will be intercepted? Since the force field is conservative, all the ions striking the surface will carry the same kinetic energy. By setting up the conservation equations for the total energy and for the angular momentum of the system, it is possible to solve for the kinetic energy of the ions striking as a function of initial ion velocity (or potential) and wire potential. Using the coordinates shown in figure 24, these equations are as follows:

$$\frac{\mu U_0^2}{2} + \frac{e V_w D}{2Z} = \frac{\mu U^2}{2} + \frac{e V_w D}{2z} \quad (\text{B13})$$

$$\mu U_0 \frac{YZ}{2L} = \mu U_\theta z \quad (\text{B14})$$

The special case of interest can be summarized as follows: $z = \frac{1}{2} D$, $U = U_\theta$, and $Y = Y_c$. As $L \rightarrow \infty$, these equations may be solved to yield the following relations:

$$\frac{Y_c}{D} = \sqrt{1 - \frac{V_w}{V_i}} \quad (\text{B15})$$

and

$$Q_B = a_c D l j V_i \left(1 - \frac{V_w}{V_i} \right)^{3/2} \quad (\text{B16})$$

If the hot wire is grounded ($V_w = 0$), equation (B16) gives the cross-sectional area and power

intercepted for the neutral-particle analysis. Furthermore, unless the wire is biased to a potential of greater than 3 percent of that of the ion accelerator, equation (B16) is correct to within 5 percent. As is discussed in appendix C, it is unlikely that the cross-sectional area used in the present analysis need ever be modified, unless a deliberate attempt is made to bias the probe.

Accommodation coefficient and sputtering theory.—The accommodation coefficient used here is defined in the classical manner (ref. 14) as

$$a_c = \frac{W_i - W_r}{W_i - W_w} \quad (\text{B17})$$

The discussion concerning the development of equation (B12) repeatedly uses the fact that $W_i \gg W_w$. Thus, for the high-energy ion-beam problem, equation (B17) reduces to

$$1 - a_c = \frac{W_r}{W_i} \quad (\text{B17a})$$

The interaction of a high-energy ion with a surface is far from completely understood. However, certain aspects of the problem have been investigated both analytically and experimentally, and it is possible to make some preliminary generalizations. The ratio of the total reflected energy to incident energy can be written as a sum of energy ratios for the various forms of "reflected" energy. Each of these energy ratios can be expressed as a product of a coefficient and a partial-energy ratio per incident ion:

$$1 - a_c = S \frac{w_{sp}^0}{w_i} + R_r \frac{w_r^+}{w_i} + K^+ \frac{w_{sec}^+}{w_i} + K^- \frac{w_{sec}^-}{w_i} + \gamma_{el} \frac{w_{el}^-}{w_i} \quad (\text{B18})$$

where S is the sputtering ratio or the ratio of the number of neutral particles emitted per incident ion, and w_{sp}^0/w_i is the ratio of the average energy of each neutral particle sputtered divided by the energy of each incident ion. Similarly, primary ions may be reflected (R_r), secondary positive ions (K^+) and negative ions (K^-) may be emitted, and secondary electrons (γ_{el}) may also be emitted. Each of these modes of "reflected" energy is considered here in turn.

The sputtering interaction of 1- to 20-kilovolt heavy ions with metals is reviewed in reference 15.

The model presented in reference 15 is well supported by experimental data which qualitatively agree with theoretical predictions. The incoming ion penetrates the metal crystal and dislodges and imparts kinetic energy to some of the crystal atoms. These atoms in turn "diffuse" through the crystal and impart energy to the atoms in their path. This multicollision process results in some of the crystal atoms receiving sufficient energy to escape. The loss of these metal atoms is commonly referred to as sputtering. The magnitude of S depends to a large extent on the velocity, mass, and angle of incidence of the incoming ion and on the crystal structure of the surface. The data summarized in reference 15, and limited experience at this laboratory, indicate that $1 < S < 10$ may be expected. No measurements of w_{sp}^0/w_i are available in the literature, but the theory (ref. 15) predicts $w_{sp}^0 \approx 20$ electron volts. Since the incident ions are in the 1000- to 20,000-electron-volt range, the magnitude of the overall sputtered energy term $\left(S \frac{w_{sp}^0}{w_i}\right)$ is small, probably less than 0.1.

An important component of the "reflected" energy is attributable to primary ions which are scattered by the surface. Reference 16 presents measurements of R in 10- to 40-kilovolt beams of various ions (H^+ , He^+ , Ne^+ , Ar^+ , Kr^+ , and O^+) for tantalum, tungsten, copper, and iron targets. Although not quantitatively applicable to the present problem, the data show that $0.01 < R_r < 0.10$ may be expected. No measurements of w_r^+ are available, but the experimental method of reference 16 presumes $w_r^+ \approx w_i$. However, the data of reference 17 showed $R < 0.01$ for positive cesium ions, which had been accelerated from 2 to 4 kilovolts, bombarding clean molybdenum surfaces. Thus, the contribution of the reflected

primary ions $R_r \frac{w_r^+}{w_i}$ may be as great as 0.10.

The secondary ion emission, both positive and negative, is also reported in reference 16. Both K^+ and K^- were found to be between 0.01 and 0.05. Furthermore, reference 18 reported measurements of w_{sec}^+ for the secondary ions from tantalum and molybdenum surfaces bombarded by 900- to 2150-volt positive cesium ions. These data show $30 < w_{sec}^+ < 50$ volts. Thus, although K^+ and K^- are not negligible and would affect a current density measuring probe such as a Faraday cup,

the energy components due to secondary ions, $K^+ \frac{w_{sec}^+}{w_i}$ and $K^- \frac{w_{sec}^-}{w_i}$, are negligible.

Secondary electron emission has been studied by many investigators. Reference 16 reports $0.05 < \gamma_{el} < 3.0$. Reference 19 states that w_{el}^- was generally less than 30 volts when various metals were bombarded by 43,000- to 426,000-volt He^+ ions. Thus, it is probably safe to neglect the energy component of secondary electrons.

In summary, a_c is no smaller than 0.8 for the hot-wire-calorimeter application to ion rocket research, and $0.9 < a_c < 1.0$ seems more probable.

Another practical consequence of sputtering is the change in diameter of a hot wire due to prolonged exposure to an ion beam. This change in diameter results, of course, in a shift of the calorimeter calibration, since the calibration is sensitive to wire diameter. The mass loss from a wire is easily related to the sputtering ratio S by the equation

$$-\frac{dm_w}{dt} = \left(\frac{M_w \pi D l}{\mathcal{F}} \right) S j \quad (\text{B19})$$

but,

$$\frac{dm_w}{dt} = \frac{\rho l \pi D}{2} \frac{dD}{dt} \quad (\text{B20})$$

Combining equations (B19) and (B20) gives

$$-\frac{dD}{dt} = \left(\frac{2M_w}{\mathcal{F}\rho} \right) S j \quad (\text{B21})$$

Equation (B21) is used in appendix C to interpret measured diameter changes in terms of the sputtering ratio S . It should be emphasized that equation (B21) implicitly assumes that the wire will sputter uniformly around the wire diameter. This is not expected to be realized experimentally, because the sputtering ratio S can be a strong function of incidence angle of the ions (ref. 15). The sputtering ratios calculated from equation (B21) must be considered in this light.

STEADY-STATE ANALYSIS

Transverse cylinder analysis.—The following section completes the steady-state analysis by presenting the analytical detail. The combination of equations (1) to (4) results in the following differential equation:

$$\frac{4}{\pi D^2} \sigma I^2 [1 + \alpha(t_w - 273)] + a_c D j V = -\frac{\pi D^2}{4} K \frac{d^2 t_w}{dx^2} \quad (\text{B22})$$

Rearrangement yields equation (5) of the text

$$\frac{d^2 t_w}{dx^2} + \beta^2 t_w = -\beta_1^2 \quad (\text{B23})$$

This equation can be reduced to the following homogeneous differential equation by a change of variable:

$$\theta = \left(\frac{\beta_1}{\beta} \right)^2 + t_w = T_{w,\infty} + t_w \quad (\text{B24})$$

Equation (B23) in terms of the variable θ is

$$\frac{d^2 \theta}{dx^2} + \beta^2 \theta = 0 \quad (\text{B25})$$

The boundary conditions are

$$\left. \begin{array}{l} t_w = T_s \\ \theta = T_{w,\infty} + T_s \end{array} \right\} \text{ at } x = \pm (l/2)$$

A solution fitting these conditions can be obtained by a method for solving ordinary, homogeneous differential equations with constant coefficients which is outlined in many texts (e.g., ref. 20). The result in terms of θ is

$$\theta = \frac{T_{w,\infty} + T_s}{\cos \frac{\beta l}{2}} \cos \beta x \quad (\text{B26})$$

Equation (6) of the text is equivalent to equation (B26).

The linear approximation (eq. (9)), which can be readily derived from equations (7) and (8), is developed as follows:

$$T_w - T_s = (T_{w,\infty} + T_s) \left[\frac{\tan \frac{\beta l}{2}}{\frac{\beta l}{2}} - 1 \right] \quad (\text{B27})$$

Considering the bracketed portion of the equation and replacing the tangent by its power series approximation yield

$$\left[\frac{\tan \frac{\beta l}{2}}{\frac{\beta l}{2}} - 1 \right] = \frac{1}{\beta l} \left[\frac{\beta l}{2} + \frac{1}{3} \left(\frac{\beta l}{2} \right)^3 + \frac{2}{15} \left(\frac{\beta l}{2} \right)^5 + \frac{17}{315} \left(\frac{\beta l}{2} \right)^7 + \dots - \frac{\beta l}{2} \right] \quad (\text{B28})$$

For $\frac{\beta l}{2} < 9^\circ$, equation (B28) is within 1 percent of the true value if only the first two terms of the series are used:

$$\left[\frac{\tan \frac{\beta l}{2}}{\frac{\beta l}{2}} - 1 \right] = \frac{1}{3} \left(\frac{\beta l}{2} \right)^2 \quad \left(\frac{\beta l}{2} < 9^\circ \right) \quad (\text{B29})$$

Combining equations (B27) and (B29) and re-writing the symbols in terms of the primary constants give the following:

$$T_w = \frac{1}{3\pi} \frac{a_c l^2}{KD} jV + \left[\frac{4}{3\pi^2} \frac{l^2}{D^4} \frac{\sigma\alpha}{K} I^2 \left(\frac{1}{\alpha} + T_s - 273 \right) + T_s \right] \quad (\text{B30})$$

Combining equation (B30) with equation (8) of the text yields the desired simplified beam sensitivity relation (eq. (9)).

Steady-state analysis for yawed wire.—To complete the detailed steady-state analysis, consider the free-molecule flow analysis for a yawed wire shown in sketch (b). The inclusion of the angle of yaw γ between the wire axis and the ion velocity vector modifies the original derivation as outlined by the following equations (ref. 7):

$$h = \frac{p v_m a_c}{(0.987 \times 10^{-5}) 2\pi^{3/2} T_i} g^o(s \sin \gamma) \quad (\text{B31})$$

$$s \sin \gamma = \frac{U \sin \gamma}{v_m} \quad (\text{B32})$$

$$h = \frac{a_c v U \sin \gamma}{(0.987 \times 10^{-5}) 2\pi^{3/2} T_i} \frac{g^o(s \sin \gamma)}{s \sin \gamma} \quad (\text{B33})$$

$$\frac{g^o(s \sin \gamma)}{s \sin \gamma} = 4\sqrt{\pi} \quad (s \sin \gamma > 4) \quad (\text{B34})$$

$$h = \frac{2a_c \mathcal{H}}{\pi M_i} \rho U \sin \gamma \quad (\text{B35})$$

$$\rho U \sin \gamma = j \left(\frac{M_i}{\mathcal{H}} \right) \sin \gamma \quad (\text{B36})$$

$$h = \left(\frac{2a_c \mathcal{H}}{\pi \mathcal{H}} \right) j \sin \gamma \quad (\text{B37})$$

Recovery temperature

$$T_e = \frac{T_i f^2 (s \sin \gamma)}{T_i g^o(s \sin \gamma)} T_i \quad (\text{B38})$$

$$T_e = \frac{5}{4} T_i \quad (s \sin \gamma > 4) \quad (\text{B39})$$

$$T_e = \frac{5 U^2}{4 2c_p} \quad (\text{B40})$$

$$T_e = \frac{1}{2} \frac{\mathcal{H}}{\mathcal{H}} V \quad (\text{B41})$$

Heat flux per unit length from beam

$$q_B = a_c D j V \sin \gamma \quad (\text{B42})$$

TRANSIENT ANALYSIS

The method for solving equation (27)

$$\frac{\rho c}{K} \frac{\partial t_w}{\partial t} = \frac{\partial^2 t_w}{\partial x^2} + \beta^2 t_w + \beta_1^2 \quad (\text{B43})$$

is outlined here. Using a change of variable (eq. (B24)) simplifies the equation to the following:

$$\frac{\rho c}{K} \frac{\partial \theta}{\partial t} = \frac{\partial^2 \theta}{\partial x^2} + \beta^2 \theta \quad (\text{B44})$$

The boundary conditions which are used are

$$(1) \text{ and } (2) \quad \theta = T_{w,\infty} + T_s \quad \text{at } x = \pm (l/2) \text{ for all } t$$

$$(3) \quad \left. \begin{aligned} \theta &= \frac{T_{w,\infty} + T_s}{\cos \frac{\beta_0 l}{2}} \cos \beta_0 x \\ \text{where } \beta_0 &\equiv \sqrt{\left(\frac{4}{\pi I^2} \right)^2 \frac{\sigma\alpha}{K} I_0^2} \end{aligned} \right\} \text{at } t=0 \text{ for all } x$$

The solution to be found is for the transient response of the wire $\theta(x,t)$ from an initial current I_0 to a current I by a step change. Following the general method of solution outlined in reference 20 (p. 231), assume a solution of the following form:

$$\theta(x,t) = u(x) + v(x,t) \quad (\text{B45})$$

The steady-state solution $u(x)$ is found in the earlier analysis to be

$$u(x) = \theta(x) = \frac{T_{w,\infty} + T_s}{\cos \frac{\beta l}{2}} \cos \beta x \quad (\text{B46})$$

In order to find the time-dependent solution, it is convenient to make another change of variable:

$$\left. \begin{aligned} w(x,t) &\equiv v(x,t)e^{-t/\tau} \\ \tau &\equiv \frac{\rho c}{K} \frac{1}{\beta^2} \end{aligned} \right\} \quad (\text{B47})$$

Substituting equations (B45) to (B47) into equation (B44) reduces the equation to be solved to a form which is readily handled:

$$\frac{1}{\beta^2} \frac{\partial^2 w}{\partial x^2} = \tau \frac{\partial w}{\partial t} \quad (\text{B48})$$

The boundary conditions in terms of the variable $w(x,t)$ are

$$(1) \text{ and } (2) \quad w=0 \quad \text{at } x=\pm l/2 \text{ for all } t$$

$$(3) \quad w = (T_{w,\infty} + T_s) \left(\frac{\cos \beta_0 x}{\cos \frac{\beta_0 l}{2}} - \frac{\cos \beta x}{\cos \frac{\beta l}{2}} \right) \quad \text{at } t=0 \text{ for all } x$$

Following reference 20 (p. 240), assume a solution having the following form:

$$\left. \begin{aligned} w &= \sum_{n=0}^{\infty} C_n e^{\frac{\lambda_n^2 t}{\beta^2 \tau}} \cos \lambda_n x \\ \lambda_n &= \frac{2}{l} \left(n\pi + \frac{\pi}{2} \right) \end{aligned} \right\} \quad (\text{B49})$$

and

$$C_n = \frac{2}{l} \int_{-l/2}^{l/2} (T_{w,\infty} + T_s) \left(\frac{\cos \beta_0 x}{\cos \frac{\beta_0 l}{2}} - \frac{\cos \beta x}{\cos \frac{\beta l}{2}} \right) \cos \lambda_n x \, dx \quad (\text{B50})$$

Completing the indicated integration of equation

(B50) in x results in the following coefficient equation:

$$C_n = 2(-1)^n (T_{w,\infty} + T_s) \left(\frac{2}{\lambda_n l} \right) \left(\frac{\lambda_n^2}{\beta^2 - \lambda_n^2} - \frac{\lambda_n^2}{\beta_0^2 - \lambda_n^2} \right) \quad (\text{B51})$$

Substituting equation (B51) into equation (B49) and using equations (B24) and (B45) to (B47) give the desired transient solution

$$t_w + T_{w,\infty} = (T_{w,\infty} + T_s) \left\{ \frac{\cos \beta x}{\cos \frac{\beta l}{2}} + \sum_{n=0}^{\infty} 2(-1)^n \left(\frac{2}{\lambda_n l} \right) \left[\frac{\lambda_n^2}{\beta^2 - \lambda_n^2} - \frac{\lambda_n^2}{\beta_0^2 - \lambda_n^2} \right] e^{-\left[\frac{\lambda_n^2}{\beta^2} - 1 \right] \frac{t}{\tau}} \cos \lambda_n x \right\} \quad (\text{B52})$$

Averaging this equation over x from $-(l/2)$ to $+(l/2)$ gives equation (28) of the text.

Equation (B52) and its length-average counterpart, equation (28), were derived for a step change in wire detection current at constant ion-beam power. However, the application of hot-wire calorimeters to transient ion-beam studies would probably be at either constant detection current or constant wire temperature. It is necessary to repeat the preceding analysis using a step change in beam power as the initial condition. This analysis has been made and the results of this additional case are summarized in the following sentences without analytical detail. The time constant of the hot-wire calorimeter was unaffected by this change in the mode of power input; τ_E of equation (29) is as good an approximation for this case as it was for the step current example. Only the coefficient C_n in equation (B51) is altered by the change in power input from detection current to beam power. Since this amplitude factor C_n is unimportant to the transient application, the analysis is not repeated here.

APPENDIX C

SOME PRACTICAL PROBLEMS IN OPERATION

As noted previously, the present probe operation in ion beams was of a demonstrative nature. The probe design was simple, rather than exact, so that there is room for improvement. For example, the probe case could be made of a non-conductor. No doubt better designed probes and survey systems will eliminate some of the problems encountered in the present study.

PROBE DESIGN

The design of an electrically insulated, water-cooled probe for operation in a vacuum is not a simple problem. However, the problem is one of technique and should be overcome with experience. The present probe design is only partly successful in meeting the requirements of good thermal conduction and electrical insulation. Resistance R_G of the present probes was only 5000 to 10,000 ohms between circuit and ground. Figure 25 shows R_G in a schematic circuit diagram. Thus, it was never possible to obtain data with a truly floating probe, which implies $R_G \rightarrow \infty$. It is possible to state that, over this limited range of probe isolation, no evidence of any effect on the measurements was noted.

The present probe was designed so that the temperature of the wire supports could be held constant by water cooling. However, as noted in

figures 16 and 17, the heating of the prongs definitely influenced the data. By recording the support thermocouple output, it is possible to compute theoretically the zero shift for any given profile. Figure 26 shows a profile in which the zero curve was computed, and the calculation may be compared with the observed data at several points of the trace. It is apparent from figure 26 that the support temperature shift can be accounted for quite accurately, so if elimination of support heating does not prove feasible, the temperature shift may be taken into account. Figure 27 shows the apparent power density attributable to the zero shift due to support heating that might be expected for some typical detection currents for a wire used in the present measurements. The probe sensitivity (i.e., the slope of the constant-current calibration lines shown in fig. 2) is not affected by a change in support temperature, so the wire calibration remains constant across the survey; only the zero point shifts.

WIRE OPERATION

Several problems have been briefly mentioned in connection with the wire calibration in the section RESULTS AND DISCUSSION. The effect of radiation from the wire was theoretically estimated, and the effect of sputtering was noted for the data of figure 16. It was also pointed out that the exact solution could be simplified, so that the wire could be calibrated directly from physical measurements. These particular problems and how to deal with them are now examined.

To show how the simplified theory (eq. (9)) suffices for practical probe designs, the data for the wire which was used to obtain the profiles shown in figure 16 are considered. A plot of R against I^2 for this wire before the run and after the run is shown in figure 28. Theory summarized by equation (9) predicts that the data should define a straight line in a plot such as figure 28. Empirical lines fitted to the data are shown for the calibrations. The intercept of one of these straight lines at $I^2=0$ is the resistance of the wire

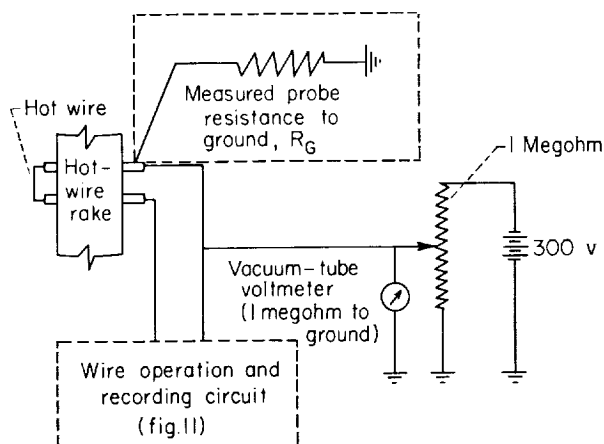


FIGURE 25.—Circuit used to vary probe potential.

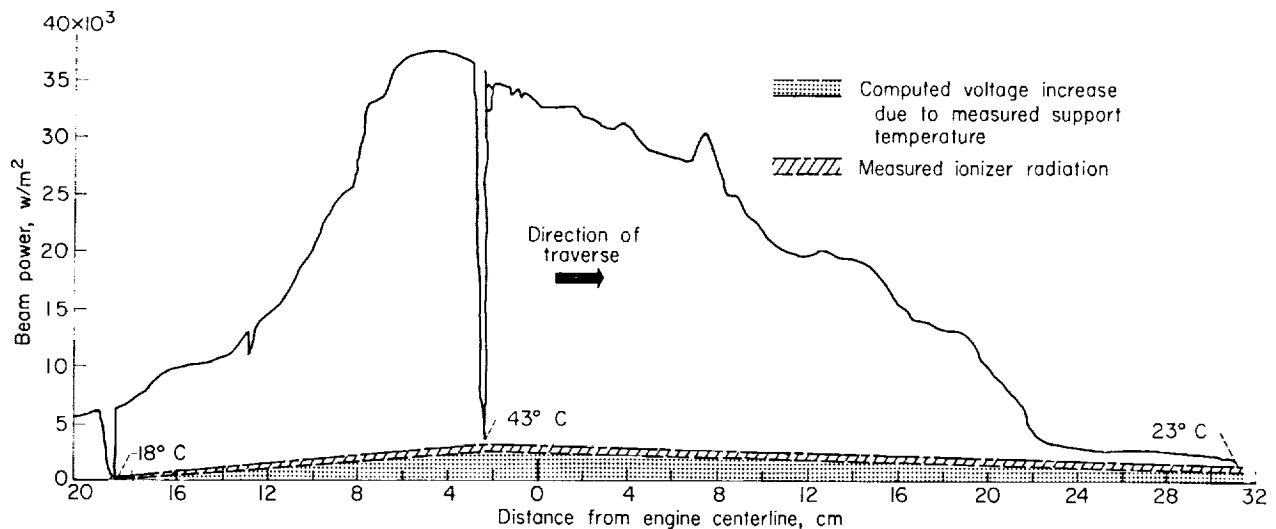


FIGURE 23.—Correction calculations for support heating compared with measurements.

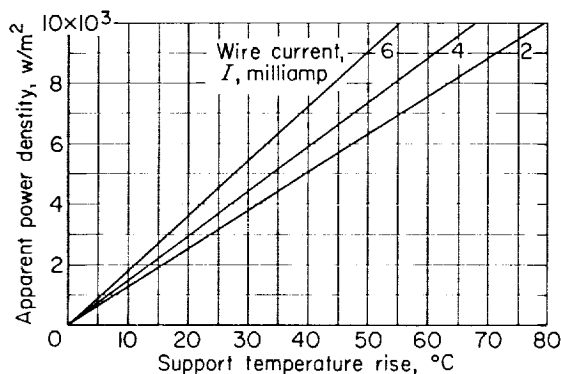


FIGURE 27.—Apparent power density output due to increase in wire support temperature. Wire diameter, 0.00127 centimeter; length, 0.508 centimeter.

at the support temperature R_s . Since all the other physical properties are known, including the measured length, the intercepts may be used to calculate an average wire diameter by the equation

$$D^2 = \frac{4\sigma l}{\pi R_s} [1 + \alpha(T_s - 273)] \quad (C1)$$

The diameters calculated in this manner are listed in figure 28 as 0.00121 centimeter before the run and 0.00106 centimeter after the run.

The slope of the calibrations may be written from equation (9) as follows:

$$\text{Slope} = \frac{4^2 \sigma^2 \alpha l^3}{3\pi^3 K D^6} [1 + \alpha(T_s - 273)] \quad (C2)$$

Once again, all physical properties are known, so that the empirical slopes can be used to calculate diameters. The ratio of the before to after slope is 0.46 for the measured calibrations. The ratio of the calculated diameters obtained from intercepts raised to the sixth power is 0.44. This is a very sensitive test of agreement between the calibrations and theory, and this example shows that excellent agreement can be expected. Furthermore, these data support the implicit assumption, which is made in this example, that the wire physical properties are unaffected by the sputtering process.

The intermediate data points between the complete calibrations shown in figure 28 may be used to calculate an average diameter at the time shown. This average diameter will suffice for a theoretical calculation of the calibration in each case. That is, equation (9) evaluated at $jV=0$ may be written as

$$R = \frac{4\sigma l}{\pi D^2} [1 + \alpha(T_s - 273)] + \frac{4^2 \sigma^2 \alpha l^3}{3\pi^3 K D^6} [1 + \alpha(T_s - 273)] I^2 \quad (C3)$$

The only unknown is wire diameter when a single wire resistance-current data point is measured. The complete calibration lines calculated from the single data points are shown in figure 28.

The sputtering case just cited is far more severe than would ever be encountered in general operation. The probe was in the beam for the total

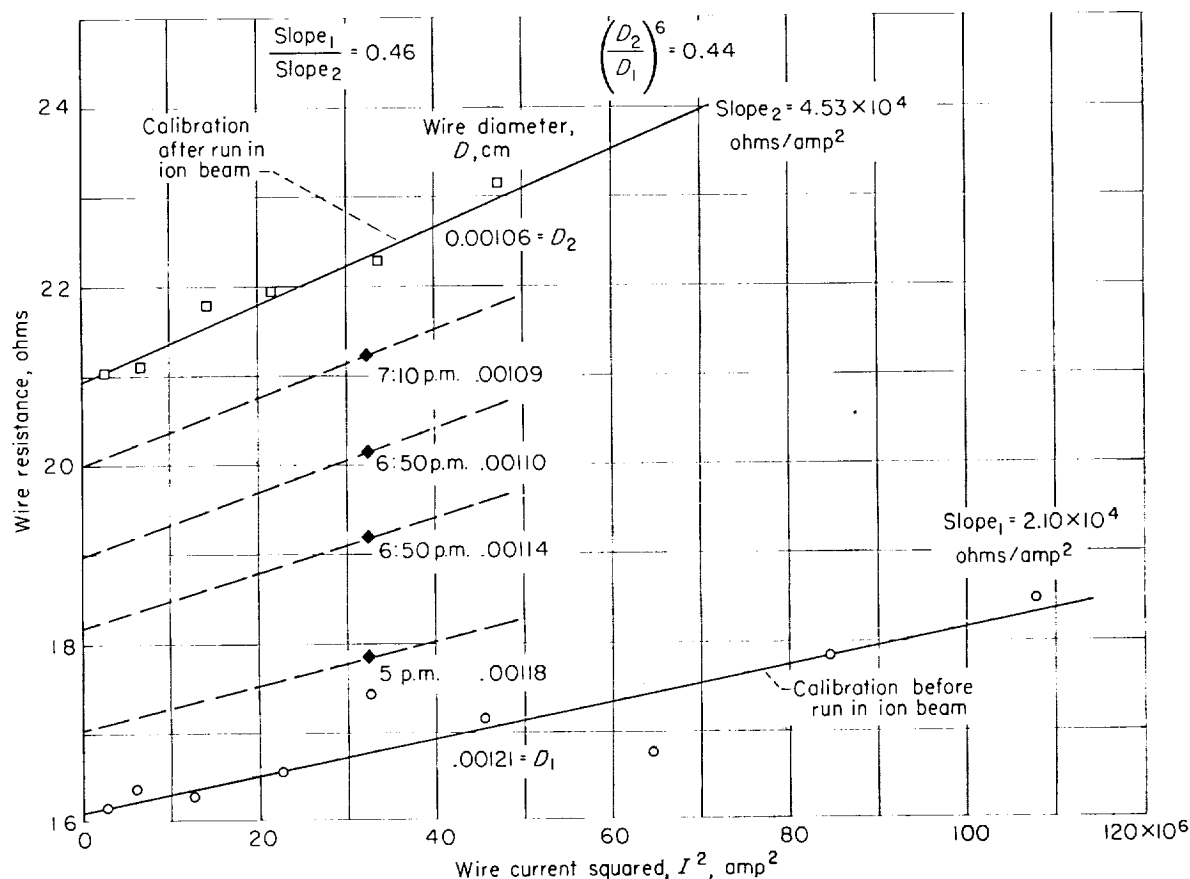


FIGURE 28.—Wire calibration and sputtering corrections available from wire measurements. Platinum-iridium wire; length, 0.513 centimeter.

time indicated in the plot. Actually the wire was in the beam longer than indicated in figure 28, as the wire started at a diameter of 0.00130 centimeter, and after removal from the tank the diameter had decreased to 0.000960 centimeter. Present operation techniques require that the wires be shielded completely from the beam, except when a survey is taken. Furthermore, the wires sweep very quickly through the beam, which greatly reduces both the sputtering and support heating problems. With these precautions little sputtering is encountered.

The radiation of heat from the hot wire to the surroundings constitutes a source of error in the present analysis. It is evident from the theoretical calculations that the radiation error will be greatly affected by wire length. Both wire length and temperature must be made small to avoid radiation errors. As a demonstration of the concepts, a set of four wires of different lengths

was calibrated. Figure 13 shows a plot of R against I^2 for four platinum-iridium wires of different lengths. These measurements are compared with the computed curves neglecting radiation. The deviation of the curves from the data indicates the current for which radiation errors are appreciable. Thermal radiation must be considered in the evaluation of thermal conductivity K , as in figure 14. It is evident that for an accurate evaluation of K a method would be to measure with decreasing wire lengths and thereby determine the maximum length for which radiation is negligible for an appreciable current range.

The problem of radiation from the hot ionizer grids of the engine to the hot-wire calorimeter needs to be evaluated for each operation. The present method of evaluating engine radiation is to take a survey with the emitters heated, but with no cesium flowing. Figures 16 and 20 give an idea of the radiation problem encountered in

several different types of engines. For practical application it is necessary that the thermal radiation from the engine does not overwhelm the ion-beam power, which of course is also a necessary condition for an efficient engine.

STRAY CURRENTS

Several sources of extraneous currents may be encountered in the present application. With the large temperature gradients encountered in the beams, care must be taken to eliminate any possible thermoelectric effects within the probes due to unsymmetrical electrical connections of unlike metals. For the present work copper leads were maintained throughout the circuit within the tank.

The wire supports must be symmetrical in area. No portion of the conductors should be unnecessarily exposed to the beam. Any exposure to the beam can lead to secondary electron emission, which may give rise to unwanted potential differences within the hot-wire circuit. On occasion it has been found that an extra drop of solder on one support could render a probe useless. Stray currents are readily checked by simply reversing the wire leads while the wire is in the beam. Reversing switches are used with every wire and should be checked at the start of each run. One could, of course, use a reversing switch to correct for the stray currents, but it appears that proper care in maintaining symmetry and in minimizing electrical conductors exposed to the beam can eliminate the problem.

The current required to neutralize the ions at the wire is of the order of 0.00001 ampere (in a 200 amp/m² beam). For the present wire tests the heating current was always greater than 0.001 ampere; thus this neutralizing current was negligible.

SPUTTERING

At the ion energies encountered in the present measurements sputtering of the wire material can occur. An example of sputtering is shown in figure 28. The knowledge of sputtering is limited (ref. 15), and nearly nonexistent for heavy ions such as cesium. The wire diameter and ion-beam power can be measured at the same time; thus very accurately controlled sputtering data can be obtained for the cylindrical geometry.

Photomicrographs of a set of five wires which correspond to probe positions similar to those in figure 19 are shown in figure 29(a). The top and

bottom probes show stains. The center wires have sputtered, apparently most heavily along longitudinal lines, which may represent grain alignment in the wires. It is necessary to establish that the staining and sputtering would not affect the wire physical properties.

Figure 23 indicates an agreement of calculated intercepts and slopes between the before and after data, which certainly suggests that the physical wire properties were unaffected by the cesium and sputtering. A somewhat more controlled check was made with a wire in a 5000-watt-per-square-meter beam for approximately 50 minutes. The original wire diameter (computed from measured length and wire resistance) was 0.00125 centimeter. After the run, the actual optically measured diameters parallel to the beam and normal to the beam were 0.00103 and 0.000996 centimeter, respectively, as shown in figure 29(b). The average diameter computed from length and measured resistance after the run was 0.00102 centimeter. These data show that the wire resistivity is unaffected by exposure to the ion beam.

The average reduction in diameter can be used to estimate the average number of atoms that must leave the wire for every ion that strikes the wire. From appendix B, equation (B21),

$$S = \frac{\Delta D}{1.90 \times 10^{-10} j t} \quad (34)$$

where ΔD is the reduction in diameter, j is the current density of the beam, and t is the time in the beam. The constant is for the platinum-iridium wire. The average sputtering ratio for the cylinder S is determined to be 5.4 atoms per ion in the 16-kilovolt cesium beam. The value of S is of the same order of magnitude as values obtained for positive silicon ions on copper at a 50° angle of incidence (ref. 15) for the same ion energy.

Comparative studies on different wire materials should perhaps improve the understanding of such effects as sputtering. A great deal of future study is necessary, particularly on the precise accommodation coefficient for the energy exchange problem.

PROBE BIAS

As noted earlier in the discussion on probe design, the resistance between the probe circuit and ground is only 5000 to 10,000 ohms. The operation of a truly floating probe has yet to be investigated. It is of interest to demonstrate that changing the floating potential of the probe



Sample as received



Wire A - pitted and stained



Wire B - pitted; fairly rough



Wire C - slightly pitted



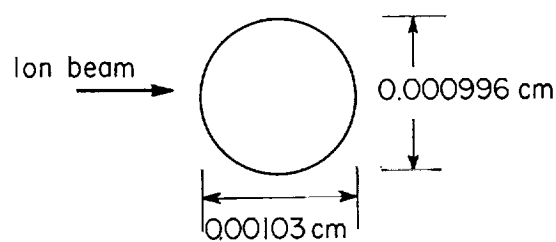
Wire D - pitted; rough



Wire E - smooth; stained

(a)

C-55383



(b)

- (a) Wires after operation in ion beam (top surface highlighted). $\times 750$. (See fig. 18 for approximate location of wires.)
 (b) Diameter measurements after run. Original measured diameter, 0.00125 centimeter; diameter after run computed from resistance, 0.00102 centimeter.

FIGURE 29.—Hot-wire sputtering observations.

over some limited range around probe operating conditions will not affect the measurements. Some limited attempts were made to explore the bias problem. Over a range of ± 50 volts the shape of the survey did not change with bias in a

beam accelerated 16 kilovolts. However, the wire current could not be maintained at a fixed value, so that an uncertainty exists in the wire calibration. The need for a truly floating probe is evident if the effect of bias is to be studied.

REFERENCES

1. Moeckel, Wolfgang E., Baldwin, Lionel V., English, Robert E., Lubarsky, Bernard, and Maslen, Stephen H.: Satellite and Space Propulsion Systems. NASA TN D-285, 1960.
2. Childs, J. H.: Design of Ion Rockets and Test Facilities. Preprint 59-103, Inst. Aero. Sci., 1959.
3. Keller, T. A.: NASA Electric Rocket Test Facilities. Paper presented at Nat. Vacuum Symposium, Cleveland (Ohio), Oct. 1960.
4. Dangle, E. E., and Lockwood, D. L.: NASA Experimental Research with Ion Rockets. Preprint 1126-60, Am. Rocket Soc., Inc., 1960.
5. Kaufman, Harold R.: One-Dimensional Analysis of Ion Rockets. NASA TN D-261, 1960.
6. Brewer, G. R., Etter, J. E., and Anderson, J. R.: Design and Performance of Small Model Ion Engines. Preprint 1125-60, Am. Rocket Soc., Inc., 1960.
7. Baldwin, L. V., Sandborn, V. A., and Laurence, J. C.: Heat Transfer from Transverse and Yawed Cylinders in Continuum, Slip, and Free Molecule Air Flows. ASME Trans. Jour. Heat Transfer, ser. C, vol. 82, no. 2, May 1960, pp. 77-87.
8. Gubareff, G. G., Ko, Shao-Yen, and McNall, P. E.: Review of the Thermal Radiation Property Values for Metals and Other Materials. GR 2462-R3, Minneapolis-Honeywell Regulator Co., May 1956.
9. Childs, J. Howard, and Mickelsen, W. R.: Grid Electrode Ion Rockets for Low Specific Impulse Missions. Paper presented at Second AFOSR Symposium on Advanced Prop. Concepts, Boston (Mass.), Oct. 7-9, 1959.
10. Kaufman, H. R., and Reader, P.: Experimental Performance of an Ion Rocket Employing an Electron Bombardment Ion Source. Preprint 1374-60, Am. Rocket Soc., Inc., 1960.
11. Baldwin, Lionel V.: Slip-Flow Heat Transfer from Cylinders in Subsonic Airstreams. NACA TN 4369, 1958.
12. Lowell, Herman H.: Design and Applications of Hot-Wire Anemometers for Steady-State Measurements at Transonic and Supersonic Airspeeds. NACA TN 2117, 1950.
13. Stalder, Jackson R., Goodwin, Glen, and Creager, Marcus O.: A Comparison of Theory and Experiment for High-Speed Free-Molecule Flow. NACA Rep. 1032, 1951. (Supersedes NACA TN 2244.)
14. Kennard, Earle H.: Kinetic Theory of Gases. McGraw-Hill Book Co., Inc., 1938, pp. 312-315.
15. Moore, Walter J.: The Ionic Bombardment of Solid Surfaces. Am. Scientist, vol. 48, no. 2, June 1960, pp. 108-133.
16. Fogel, Ya. M., Slabospitskii, R. P., and Pastrepin, A. B.: Emission of Charged Particle from Metal Surfaces Under Bombardment by Positive Ions. Soviet Phys.-Tech. Phys., vol. 5, no. 1, July 1960, pp. 58-66.
17. Brunnée, Curt: Über die Ionenreflexion und Sekundärelektronenemission beim Auftreffen von Alkaliionen auf reine Molybdän-Oberflächen. Zs. f. Phys., bd. 147, no. 5, 1957, pp. 161-183.
18. Veksler, V. I.: Energy Distribution of Sputtered and Scattered Ions in the Bombardment of Tantalum and Molybdenum by Positive Cesium Ions. Jour. Exp. Theoret. Phys. (USSR), vol. 38, Feb. 1960, pp. 324-334. (English trans. in Soviet Phys. JETP, vol. 11, no. 2, Aug. 1960, pp. 235-242.)
19. Hill, A. G., Buechner, W. W., Clark, J. S., and Fisk, J. B.: The Emission of Secondary Electrons Under High Energy Positive Ion Bombardment. Phys. Rev., vol. 55, Mar. 1, 1939, pp. 463-470.
20. Wylie, C. R., Jr.: Advanced Engineering Mathematics. McGraw-Hill Book Co., Inc., 1951.
21. Hodgman, Charles D., ed.: Handbook of Chemistry and Physics. Thirty-eighth ed., Chem. Rubber Pub. Co., 1956-1957.

TABLE I.--PHYSICAL PROPERTIES OF WIRE MATERIALS

Material	Thermal coefficient of resistance, α , $1/^{\circ}\text{K}$	Resistivity, σ , (ohm) (m)	Thermal conductivity, k , w/(m) ($^{\circ}\text{K}$)	Density, ρ , kg/cu m (a)	Specific heat, c_p , j/(kg) ($^{\circ}\text{K}$) (a)
Platinum.....	^a 3.8×10^{-3}	^a 9.82×10^{-8}	^a 72.5	21,600	134
Tungsten.....	^b 4.0×10^{-3}	^b 6.98×10^{-8}	^b 160.2	19,500	128
80% Platinum -20% iridium.....	^c 8.5×10^{-3}	^c 3.28×10^{-7}	^c 17.5	21,600	134
Platinum-iridium wires used in measurements.....	^d 7.90×10^{-3}	^d 3.57×10^{-7}	^d 25.5	21,600	134

^a Ref. 21.^b Ref. 11.^c Ref. 12.^d This work.

